An Analytical Model for CO_2 Surface Forcing, with Application to the Direct Precipitation Response

Yue Xu[1,2], Daniel D. B. Koll[1], Nicholas J. Lutsko[2]

[1]Laboratory for Climate and Ocean-Atmosphere Studies, Department of Atmospheric and Oceanic Sciences, Peking University, Beijing, People's Republic of China
[2]Scripps Institution of Oceanography, University of California, San Diego, La Jolla, California, USA

Corresponding author: Daniel D. B. Koll, dkoll@pku.edu.cn

Abstract

If temperature is held constant, increasing atmospheric CO_2 reduces atmospheric radiative cooling and suppresses precipitation. Global Climate Models suggest this "direct" precipitation response ranges from -2% to -3% per CO_2 doubling, and hence contributes significantly to the net precipitation response of +3% to +9% per CO_2 doubling. Our study aims to explain the magnitude and state-dependence of the direct precipitation response by developing an analytical model for CO_2 surface forcing. The model is grounded in idealized CO_2 spectroscopy that considers CO_2 absorption bands both at 667 cm^{-1} and 1000 cm^{-1} and is validated against line-by-line radiative transfer calculations. Surface forcing increases with higher surface temperatures and less atmospheric water vapor. By combining our model with a previously established analytical model for top-of-atmosphere CO_2 forcing, we derive a simplified model to estimate atmospheric forcing and quantify the global-mean precipitation sensitivity to CO_2 changes. Atmospheric forcing increases with surface temperature and decreases with tropopause temperature. Despite ignoring shortwave changes and clouds, our analytical results compare favorably with the surface forcing in CMIP6 models and capture the bulk of these models' direct precipitation response. Our surface forcing model thus provides a theoretical understanding for how CO_2 increases suppress precipitation; it also has implications for understanding the precipitation response under solar geoengineering and how CO_2 changes affect land climates.

1 Introduction

The radiative forcing of CO_2 (F_{TOA}) refers to the reduction in longwave and shortwave radiation escaping the climate system at either the top-of-atmosphere (TOA) or at the tropopause when atmospheric CO_2 concentrations are increased and surface temperature (Ts) remains constant (Etminan et al., 2016). Increased CO_2 concentrations also increase the longwave radiation reaching the Earth's surface, known as the surface forcing (F_{surf}). F_{surf} has received less attention than F_{TOA}, yet it is intricately linked to variations in the hydrological cycle: the net atmospheric forcing (F_{atm}) is the difference between F_{TOA} and F_{surf} (Allen & Ingram, 2002; Chen et al., 2023), and is largely balanced by changes in latent heating when averaging over sufficiently large spatial scales:

$$F_{atm} = F_{TOA} - F_{surf} \approx -L\Delta P_{CO_2}. \tag{1}$$

Here, L is the latent heat of vaporization of water, ΔP_{CO_2} is the precipitation response per CO_2-doubling measured in mm/s, and all forcings are in units of $\mathrm{W/m^2}$. The relation is approximate because it omits changes in sensible heating, which are roughly three times smaller than the changes in latent heating (Siler et al., 2019), changes in shortwave fluxes as well as changes due to clouds (which we return to below). By convention downward fluxes are positive, so for an increase in CO_2 both F_{TOA} and F_{surf} are positive.

ΔP_{CO_2} is typically referred to as the "fast" or "direct" precipitation response and represents the change in precipitation when CO_2 concentrations are instantaneously increased and temperatures have yet to respond. Typically, F_{TOA} is larger in magnitude than F_{surf}, resulting in negative ΔP_{CO_2} , with climate model simulations giving values of $\sim$ -3 to -2% per CO_2 doubling. This reduction in precipitation offsets a substantial fraction of the temperature-mediated increase in precipitation, which is typically +1 to +3%/K of surface warming, or about +3 to +9% per CO_2 doubling (Andrews et al., 2010; Kvalevåg et al., 2013; Richardson et al., 2016; Myhre et al., 2017; Jeevanjee & Romps, 2018). By contrast, the "slow" or "indirect" precipitation response ΔP_{Ts} is driven by changes in surface temperature (note, equation 1 is also valid on "slow" timescales, but in this case F_{TOA} and F_{surf} are no longer equal to the radiative forcings and instead have to be replaced with the changes in TOA and surface radiative fluxes that take into account surface temperature changes). ΔP_{Ts} is generally positive, though it becomes constant, or even decreases, at high temperatures (Pierrehumbert, 2002; O'Gorman & Schneider, 2008; Liu et al., 2024).

What determines the magnitude of the direct precipitation response? The answer is currently unclear, but an improved understanding would help narrow the persistently large uncertainty in future precipitation changes (Douville et al., 2021). A clearer understanding of the direct response is also pertinent to solar geoengineering proposals. Simulations of solar geoengineering interventions typically feature residual reductions in precipitation when surface temperatures are restored but CO_2 concentrations are still high (Bala et al., 2008; K. L. Ricke et al., 2010; Seeley et al., 2021; K. Ricke et al., 2023). Blocking solar radiation lowers temperatures, and thus reverses the indirect precipitation response ΔP_{Ts} under global warming, but does not reverse the direct precipitation response ΔP_{CO_2} induced by higher CO_2 concentrations.

One way to improve our understanding of ΔP_{CO_2} is to focus on F_{TOA} and F_{surf}. Several recent papers developed analytical models for F_{TOA} based on spectral decompositions of CO_2 forcing and comparisons with line-by-line (LBL) radiative transfer calculations (Jeevanjee et al., 2021; Romps et al., 2022; Stevens & Kluft, 2023). These studies established a conceptual framework for thinking about F_{TOA} and its spatial and state dependency. Our goal in this paper is to develop an analogous model for F_{surf} to facilitate insights into the direct precipitation response of CO_2. As F_{surf} governs the responses of surface turbulent (latent and sensible) heat fluxes (Andrews & Forster, 2010; Stephens et al., 2012; Pendergrass & Hartmann, 2014), the model also has implications for studying the response of land climates to CO_2.

We develop and validate the analytical model for F_{surf} in Sections 2 and 3. We then combine it with the F_{TOA} model of Jeevanjee et al. (2021) to estimate the direct precipitation response to CO_2 forcing. Subsequently, we compare our model to the "fast" precipitation response ΔP_{CO_2} in Global Climate Models (GCMs) participating in RFMIP in Section 4. We find that our model accurately predicts the magnitude of ΔP_{CO_2} in GCMs, though further analysis suggests that the accuracy of this fit may be somewhat fortuitous and due to canceling errors. Clear-sky longwave fluxes account for about 2/3 of ΔP_{CO_2} in GCMs, while the rest ($\sim$1/3) of ΔP_{CO_2} is due to changes in clear-sky shortwave fluxes driven by changes in water vapor absorption, an effect not included in our model. We conclude in Section 5.

2 Analytical Model Preliminaries

This section outlines the conceptual framework and underlying parameterizations of our analytical model; the approach is closely related to the analytical forcing and feedback models in Jeevanjee et al. (2021) and Koll et al. (2023). We consider an isolated 1D atmospheric column. The column's state is described by its surface temperature (Ts), its tropopause temperature (T_{tp}), a bulk tropospheric lapse-rate (Γ), a bulk tropospheric relative humidity (RH), plus atmospheric CO_2 concentration. Here and in the next section we assume idealized atmospheric profiles with vertically uniform Γ and RH, while in Section 4 we derive (Ts, T_{tp}, Γ, RH) from RFMIP data.

Similar to Jeevanjee et al. (2021), our key insight is that the flux change due to a CO_2 increase can be approximated using simple geometric shapes in flux-wavenumber space. However, whereas Jeevanjee et al. (2021) only considered the contribution from the strong "main" 667 cm^{-1} band, we find that the surface forcing also requires us to consider weaker "new" bands around 1000 cm^{-1}. To express the forcing contributions of these bands analytically we use parameterizations for the shapes of the absorption spectra of CO_2 and H_2O, plus their optical thickness relations. Section 2.1 describes the vertical thermodynamic profiles in the analytical model, Section 2.2 describes parameterizations for the absorption spectra, and Section 2.3 describes parameterizations for optical thickness.

2.1 Thermodynamic Profile

We construct vertical thermodynamic profiles following Koll et al. (2023). Based on the fixed-anvil temperature (FAT) hypothesis (Hartmann & Larson, 2002), we assume a constant tropopause temperature T_{tp} fixed at 200 K, and treat stratospheric temperatures as isothermal and equal to T_{tp}. Next, we estimate the tropopause altitude Z_{tp} using the approximation from Romps (2016):

$$Z_{tp}(Ts) = \frac{1}{g}[C_p(Ts - T_{tp}) + L_v q^*_{vs}], \tag{2}$$

where g is the acceleration of gravity, C_p is the specific heat capacity of air at constant pressure, and L_v is the latent heat of condensation. q^*_{vs} denotes the surface saturation specific humidity which is set by the Clausius-Clapeyron relation, which we approximate as:

$$q^*_{vs}(Ts) = \frac{R_a}{R_v}\frac{e^*_{vs}}{Ps} = \frac{R_a}{R_v}\frac{e^*_0}{Ps}\exp\left(\frac{L_v(Ts - T_0)}{R_v T_0^2}\right). \tag{3}$$

Here, $e^*_{vs} = e^*_0 \exp\left(\frac{L_v(Ts-T_0)}{R_v T_0^2}\right)$ is the surface saturation vapor pressure; e^*_0 is a reference saturation vapor pressure at the reference temperature T_0; and R_a and R_v are the specific gas constants for dry air and H_2O, respectively.

Based on Equation 2 we define the atmospheric bulk lapse rate Γ as

$$\Gamma(Ts) = \frac{dT}{dZ} \approx \frac{\Delta T}{Z_{tp}} = \frac{g(Ts - T_{tp})}{C_p(Ts - T_{tp}) + L_v q^*_{vs}}. \tag{4}$$

Γ decreases as Ts increases because it is dominated by the latent heat term, $L_v q^*_{vs}$, which increases rapidly with Ts. Consequently, in a warmer climate, the atmospheric temperature decreases more slowly with altitude. Γ maximizes in a dry atmosphere, where it reaches $\Gamma_d = \frac{g}{C_p} \approx 10$ K/km.

2.2 Approximating the absorption spectra of CO_2 and H_2O

Previous studies of CO_2 radiative forcing focused on the optically thick 667 cm^{-1} band (500 - 870 cm^{-1}) (Jeevanjee et al., 2021; Romps et al., 2022), which is the main contributor to TOA radiative forcing. The 667 cm^{-1} band is also important for the surface forcing, but we find that two new bands must be included to model F_{surf} accurately: the left new band centered at 960 cm^{-1} (L) and the right at 1060 cm^{-1} (R) (Fehr & Krossing, 2020). These new bands are much weaker than the 667 cm^{-1} band (see Figure S1), so we provide separate models for the emission in the 667 cm^{-1} band and the new bands.

The 667 cm^{-1} band is already optically thick; therefore the main effect of increasing CO_2 is to widen the band, allowing CO_2 to radiate towards Earth's surface across a larger range of wavenumbers. Following Jeevanjee et al. (2021), the CO_2 absorption coefficient can be approximated as decreasing exponentially away from the center of the 667 cm^{-1} band. If CO_2 increases from an initial concentration q_i to a new concentration q, the range of wavenumbers that are optically thick then widens logarithmically (in wavenumber space) on each side by an amount

$$\Delta w = l_{667} ln\left(\frac{q}{q_i}\right), \tag{5}$$

where l_{667} is the exponential decay parameter of CO_2's absorption coefficient in units of cm^{-1} (Jeevanjee et al., 2021). We determine l_{667} by fitting the CO_2 absorption spectrum in Section 3.2.

The new CO_2 bands are optically thin at concentrations similar to present-day (less than 1000 ppm; see Figure S1), so the downward flux at the surface is weak. Nevertheless, the new bands' contribution to the surface forcing is not negligible because they are broad compared to changes in the width of the main CO_2 band; Figure S2 shows a representative width of $\sim$ 150 cm^{-1} for the new bands, which should be compared to $\Delta w \sim$ 7 cm^{-1} for a CO_2 doubling based on Equation and our fit for l_{667} (see Section 3).

The main effect of increasing CO_2 in the new bands is to increase the weak downward radiative flux at each wavenumber. Unlike our model of the 667 cm^{-1} band, we assume the widths of the new bands remain constant. To model the relationship between CO_2 concentration and the increase in downward radiative flux, we assume the CO_2 absorption coefficient κ^{CO_2} is dominated by pressure broadening and depends only on total atmospheric pressure P,

$$\kappa^{CO_2} = \kappa^{CO_2}_{ref} \frac{P}{P^{CO_2}_{ref}}, \tag{6}$$

where $\kappa^{CO_2}_{ref}$ has units of m^2/kg and represents the reference absorption coefficient of CO_2 for each new band at a reference atmospheric pressure $P^{CO_2}_{ref}$. We take $\kappa^{CO_2}_{ref} = 9.12\times10^{-4} m^2/kg$ for the L band, $\kappa^{CO_2}_{ref} = 1.40\times10^{-3}$ m^2/kg for the R, and $P^{CO_2}_{ref} = 10^4$ Pa. (listed in Table S1)

Next, we need to account for overlap between CO_2 bands and H_2O. Following Jeevanjee et al. (2021), we denote the spectral interval 550-600 cm^{-1} on the left side of the 667 cm^{-1} band as (-) and the interval 750-800 cm^{-1} on the right side of the band as (+) (see Figure S2). The (-) is influenced by absorption from the H_2O rotational band, while the (+) and the new bands are influenced by absorption from the H_2O continuum. Prior studies have provided estimates for the absorption coefficients of H_2O in the rotation band ($\kappa^{H_2O}_{rot}$) and continuum ($\kappa^{H_2O}_{ctn}$) (Jeevanjee et al., 2021). $\kappa^{H_2O}_{rot}$ at atmospheric pressure P is:

$$\kappa^{H_2O}_{rot} = \kappa^{H_2O}_{rot,ref} \frac{P}{P^{H_2O}_{ref}}, (-) \tag{7}$$

where $\kappa^{H_2O}_{rot,ref}$ is the reference absorption coefficient for H_2O in (-) at the reference atmospheric pressure $P^{H_2O}_{ref}$. We take $\kappa^{H_2O}_{rot,ref} = 0.15$ m^2/kg, $P^{-,H_2O}_{ref} = 6.5\times10^4$ Pa. $\kappa^{H_2O}_{ctn}$ at RH, T is:

$$\kappa^{H_2O}_{ctn} = \kappa^{H_2O}_{ctn,ref} \frac{RH}{RH_{ref}} e^{(\frac{L_v}{R_v T^2_{ref}} - \sigma)(T - T_{ref})}, (+), L, R. \tag{8}$$

Here $\sigma = 0.021$ K^{-1} is a temperature scaling coefficient. The reference temperature T_{ref} $= 275$ K, $RH_{ref} = 0.75$, $\kappa^{H_2O}_{ctn,ref} = 0.055$ m^2/kg for (+), 0.0136 m^2/kg for L new band, and 0.0176 m^2/kg for R new band.

The reference values of $\kappa^{H_2O}_{rot}$ and κ^{CO_2} are taken from HITRAN 2016 (Gordon et al., 2017), while $\kappa^{H_2O}_{cnt}$ is taken from MT_CKD_v3.2 (Mlawer et al., 2012) and rescaled to align with the values used by Jeevanjee et al. (2021). The values for the (+) and (-) bands represent averages within the respective wavenumber ranges, and the radiative properties of H_2O in the new bands are represented by values at the L band and R band centers. With these absorption coefficients, we calculate downward optical thicknesses, as discussed in the next subsection.

The reference parameters used in this study, along with the fitted parameters, are provided in Table S1. Subscripts are used to denote different bands and gases.

2.3 Downward optical thickness

We define the downward optical thickness (τ_d) as the integrated opacity of an atmospheric absorber from some level in the atmosphere down to the surface:

$$\tau_d = \int_P^{P_s} \kappa q \frac{dp}{g}, \tag{9}$$

where p is the pressure of the atmospheric level (Pa), p_s is the surface pressure (Pa), κ is the mass absorption coefficient (m^2/kg) as described in Section 2.2, and q is the mass concentration of the atmospheric absorber (kg/kg). Note that Equation 9 applies monochromatically and that τ_d decreases with increasing pressure; that is, the downward optical thickness is largest at TOA.

Plugging Equations 6–8 into Equation 9 and integrating from the TOA down to the surface, we obtain the following expressions for τ_d for CO_2 and H_2O:

$$\tau_d^{CO_2} = k_{ref}^{CO_2} \frac{q}{P_{ref}^{CO_2}} \frac{P_s^2}{2g}, \tag{10}$$

$$\tau_{d,rot}^{H_2O} = k_{rot,ref}^{H_2O} WVP_0 \frac{P_s}{P_{ref}^{H_2O}} e^{-\frac{L_v}{R_v Ts}}, (-) \tag{11}$$

$$\begin{aligned} \tau_{d,ctn}^{H_2O} \quad &= \quad \frac{RH^2 \rho_{ref}^* k_{ctn,ref}^{H_2O}}{\alpha RH_{ref}\Gamma} e^{\alpha(Ts-T_{ref})}, (+), L, R \\ \text{where,} \quad &\alpha = \frac{2L_v}{R_v T_{ref}^2} - \sigma. \end{aligned} \tag{12}$$

Here, WVP_0 is a reference column water vapor path, given by $WVP_0 = \int q^* \text{ dp/g} = (Ts + T_{tp})RHp_v^\infty/(2\Gamma L_v)$, where $p_v^\infty = 2.5 \times 10^{11}$ Pa (Koll & Cronin, 2018; Jeevanjee & Fueglistaler, 2020; Jeevanjee et al., 2021). ρ_{ref}^* is the saturated water vapor density at the reference temperature T_{ref} (kg/m^3).

Note that we do not require a model for the CO_2 optical depth in the 667 cm^{-1} band, because this band is already optically thick. Put differently, the 667 cm^{-1} band already emits from very close to the surface, so increasing CO_2 only increases the downward flux into the surface by widening the band (Δw), not by increasing the temperature from which the downward emission originates.

2.4 The Downward Radiative Flux

Finally, we approximate the atmosphere's downward radiative flux into the surface I_d. A useful upper bound on I_d can be obtained by neglecting the atmosphere's detailed temperature structure and assume it is isothermal with temperature equal to the surface temperature Ts. There is no downward longwave flux at the TOA, so the downward flux at the surface takes a modified form of Beer's law:

$$I_d = (1 - \exp(-\tau_d))\pi B(\nu, Ts). \tag{13}$$

Here $B(\nu, Ts)$ is the Planck function evaluated at wavenumber ν and temperature Ts. I_d increases with the downward optical depth τ_d. This expression is an upper bound on I_d because it uses Ts in the Planck function. In reality, unless the atmosphere had an inverted temperature structure, any downward emission originates from an atmospheric temperature that is colder than Ts.

3 Analytical Models for Surface and Atmospheric Forcing

We next describe our analytical model for the Clear-Sky Longwave (CSLW) component of F_{surf}. We begin by considering an atmosphere with CO_2 as the only greenhouse gas, then generalize the model to a moist atmosphere with both CO_2 and H_2O. Finally, we combine our model with Jeevanjee et al. (2021)'s F_{TOA} model to obtain an analytical model for atmospheric forcing F_{atm}. We test these analytical models against line-by-line radiative transfer calculations across various thermodynamic conditions and CO_2 concentrations. Similar to Jeevanjee et al. (2021), our model for F_{surf} contains two free parameters, which we tune based on line-by-line calculations.

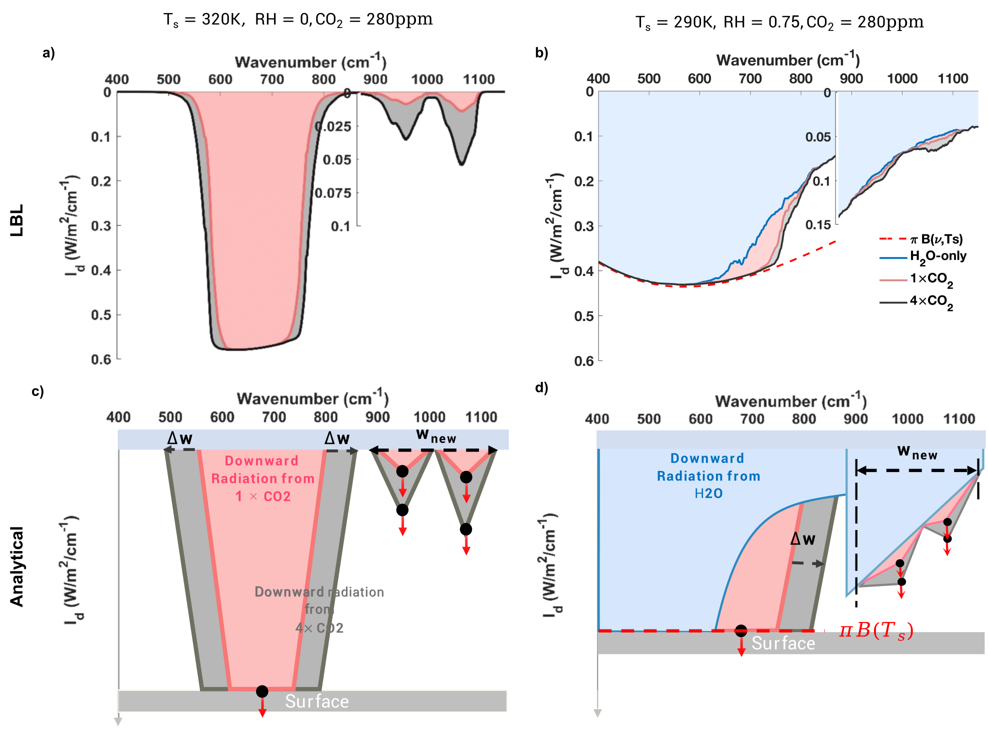

Figure 1. The downward radiative flux into the surface, I_d, at CO_2 = 280 ppm (q_i) and 1120 ppm ($4q_i$). a) Output from the PyRADS LBL model with Ts = 320 K and RH=0. b) Output from the PyRADS LBL model with Ts=290K and RH=0.75. The added blue curve represents I_d in the presence of H_2O-only. Spectra are smoothed using a 50cm^{-1} sliding window. The x-axis is split at 870cm^{-1} to illustrate the 667 cm^{-1} band and the new bands of CO_2, with a change in y-axis scale at 870cm^{-1}. Panels c) and d) are schematic diagrams of the top panels used to construct our analytic model.

3.1 PyRADS Line-By-Line model

We validate the analytical models by comparing them to line-by-line calculations with the PyRADS radiation code (Koll & Cronin, 2019). This code incorporates H_2O and CO_2 line data from HITRAN 2016 (Gordon et al., 2017), H_2O continuum data from MT_CKD_v3.2 (Mlawer et al., 2012), and CO_2 continuum data derived from a fitting function (Pierrehumbert, 2010). Doppler broadening is incorporated via a Voigt lineshape. The model's spectral range covers 0.1 cm^{-1} to 3500 cm^{-1} ,with a 0.01 cm^{-1} bin size. All calculations are conducted assuming a moist adiabatic troposphere coupled to an isothermal stratosphere at 200 K. For computational efficiency, the atmospheric layer where temperature decreases to 200 K is designated as the tropopause, while the model top is placed at 0.9 times the tropopause pressure. RH is vertically constant. For a CO_2-only atmosphere (i.e., an atmosphere where CO_2 is the only greenhouse gas), we set RH to 0%. The atmosphere is resolved using 50 vertical levels, logarithmically spaced in pressure between the surface and model top.

3.2 F_{surf} in a CO_2-only atmosphere

We first examine how the downward flux at the surface (I_d) responds to changes in CO_2. The left panels of Figure 1 illustrate an example with CO_2 as the only greenhouse gas. To better visualize the effect we set Ts = 320 K, as the new bands become more significant at higher Ts. Atmospheric CO_2 is increased from 1x to 4x the preindustrial CO_2 concentration (280 ppm); panel a) shows the results of a LBL calculation, while panel c) shows a schematic representation. In the figure, the y-axis is inverted, so emission from closer to the surface (i.e., from warmer temperatures) appear lower on the axis.

In the 667 cm^{-1} band, increasing CO_2 means a wider range of wavenumbers emit from close to the surface and fewer wavenumbers emit from close to the TOA. The flux originating very close to the surface is $\pi B(\nu_0, Ts)$, whereas the flux originating from the TOA is zero. The resulting change in flux due to a CO_2 increase is represented by the shaded gray area in Figure 1a.

Geometrically this area can be approximated by two parallelograms, each with a width of Δw and a height of $\pi B(\nu_0, Ts)$. Following Jeevanjee et al. (2021), the width Δw of the parallelograms increases by the amount specified in Equation 2.2 for each CO_2 doubling, while the height increases according to the Planck function. Note that the left and right parallelogram in Figure 1a have slightly different heights, which is due to the wavenumber-dependence of $B(\nu, T)$. However, as long as the 667 cm^{-1} band is narrow relative to the Planck function this variation can be approximated as linear and canceling between opposite band wings, so we can approximate $B(\nu, T)$ across the band by using its central value at 667 cm^{-1}. Thus, the surface forcing in the 667 cm^{-1} band, $F_{surf,667}$, is given by

$$
\begin{aligned}
F_{surf,667} &= 2\Delta w \pi B(\nu_0, Ts) \\
&= 2 l_{667} ln \left(\frac{q}{q_i}\right) \pi B(667cm^{-1}, Ts),
\end{aligned} \tag{14}
$$

where q_i and q (in units of kg/kg) are the mass concentrations of CO_2 before and after an increase, respectively, and B(667 cm^{-1}, Ts) (Wm^{-2}/cm^{-1}) is the Planck function at wavenumber 667 cm^{-1} and temperature Ts.

To estimate F_{surf} from the new CO_2 bands, $F_{surf,new}$, we focus on the increase in I_d at each wavenumber and disregard changes in bandwidth. Geometrically, the areas highlighted in Figure 1a closely resemble two triangles. An increase in CO_2 increases the height of each triangle but does not increase the length of its base (physically, this occurs because the new bands are optically thin so an increase in CO_2 primarily enhances the flux within the bands without significantly altering their bandwidths).

Due to the similar shapes of the L and R bands, we simplify the derivation by assuming that the base lengths of the two triangles are equal, each being $\frac{1}{2}w_{new}$. The heights correspond to the downward radiative fluxes in the L and R bands, denoted as I_d(L, q) and I_d(R, q), respectively. $F_{surf,new}$ is then the difference in triangle area when varying CO_2 from q to q_i:

$$
\begin{aligned}
F_{surf,new} &= \frac{1}{4} w_{new} [I_d(L, q) - I_d(L, q_i) + I_d(R, q) - I_d(R, q_i)] \\
&= \frac{1}{2} w_{new} [I_d(new, q) - I_d(new, q_i)]
\end{aligned} \tag{15}
$$

where $I_d(new, q) = \frac{1}{2}[I_d(L, q) + I_d(R, q)]$, represents the mean downward radiative flux from the new bands. This flux is calculated using Equation 13, evaluated at the center of each band.

To determine the two free parameters l_{667} and w_{new}, we conduct a set of LBL calculations with Ts ranging from 230 K to 310 K, with CO_2 = 280 ppm and CO_2 = 560 ppm.

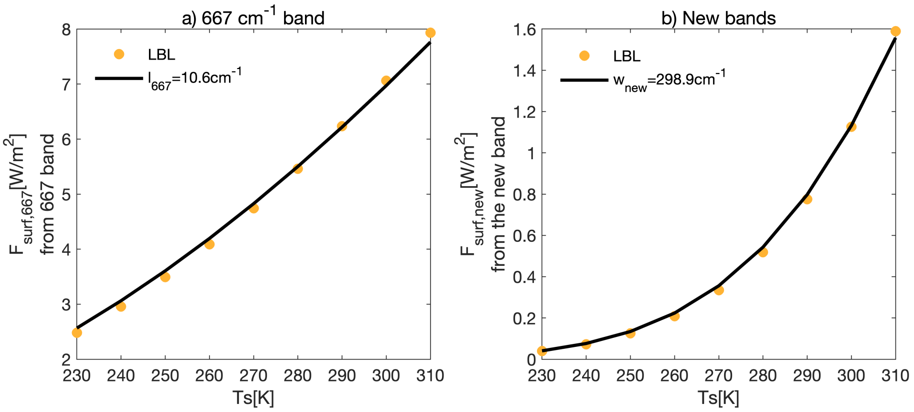

Figure 2. Fitting results for the two free parameters in the analytical model (Equation 16) compared to LBL results. To fit the parameters we assume CO_2 is the only radiatively active gas and has a concentration of 280 ppm, while Ts ranges from 230 K to 310 K. a) Surface forcing for the 667 cm^{-1} band $F_{surf,667}$. b) Surface forcing for the new bands $F_{surf,new}$. Orange dots: LBL (PyRads). Black curves: Analytical model.

From each calculation, we output $F_{surf,667}$, $F_{surf,new}$, I_d(new, q) and I_d(new, q_i). We substitute Ts and the outputted I_d(new, q) and I_d(new, q_i) into Equations 14 and 15 to obtain the estimated $F_{surf,667}$ and $F_{surf,new}$. Then we perform linear regression between the simulated and estimated $F_{surf,667}$ and $F_{surf,new}$ to determine l_{667} and w_{new}. This procedure yields optimal values of $l_{667} = 10.6$ cm^{-1} and $w_{new} = 298.9$ cm^{-1} (Figure 2). The parameter values are an excellent fit to the LBL calculations, with R^2 values close to 1.

Using the Taylor expansion, retaining only the first-order approximation, our final model for F_{surf} in a CO_2-only, clear-sky atmosphere is given by:

$$\begin{aligned} F_{surf} &= F_{surf,667} + F_{surf,new} \\ &= 2l_{667} ln(2)\pi B(667cm^{-1}, Ts) \\ &\quad +74.7cm^{-1}\pi B(1000cm^{-1}, Ts)117.9q_i \end{aligned} \tag{16}$$

The approximate conversion of the CO_2 volume fraction into its mass fraction is $q_i = PPMV_{CO_2} \times 44/29$ kg/kg. If CO_2 is the only greenhouse gas and under representative conditions (Ts=300K, 280 ppm CO_2) F_{surf} is dominated by the 667 cm^{-1} band, which contributes 3 times more to F_{surf} than the new bands. Both terms increase with Ts due to the temperature-dependence of the Planck function, but the contribution from the new bands also increases with the CO_2-abundance. At Ts=300K, the contribution from the new bands starts outweighing the contribution from the 667 cm^{-1} band above 10^4 ppm of CO_2 (Figure S3).

3.3 F_{surf} in a CO_2-H_2O atmosphere

We now generalize the model to include H_2O. The right panels of Figure 1 are similar to the left panels but with RH = 0.75 and a lower temperature Ts = 290 K, to make the strength of H_2O absorption more relevant for present-day Earth. Comparing I_d at 280 ppm with and without H_2O, the rotation band of H_2O significantly enhances I_d on the left side of the 667 cm^{-1} band, while the H_2O continuum enhances I_d on the right side of the 667 cm^{-1} band and in the new bands. At shorter wavenumbers H_2O intensifies I_d so much that the downward flux already originates from just above the surface, and adding more CO_2 no longer increases the downward emission (Figure 1d, at less than 700 cm^{-1}). In other parts of the spectrum H_2O increases I_d but the surface flux is still sensitive to increases in CO_2 (Figure 1d, above 700 cm^{-1}). In both cases, the radiative forcing of CO_2 is smaller with H_2O than in the CO_2-only case.

$F_{surf,667}$ can still be estimated using the differences between I_d in the (-) and (+) regions of the 667 cm^{-1} band and I_d emitted from the 667 cm^{-1} band center, but I_d in (-) and (+) is now equal to the downward flux emitted by the H_2O rotation band and the H_2O continuum. Under the conditions shown in Figure 1, I_d in the (-) region is so strong that the downward flux is already equal to the surface Planck function (Figure 1d), so adding CO_2 does not affect I_d. In the (+) region, the H_2O continuum produces a relatively weak I_d, allowing more CO_2 to enhance I_d and thereby contribute to a net $F_{surf,667}$. Note that if RH or Ts are lower, as shown in Figure S4, H_2O in the (-) region becomes optically thin and I_d is weaker, which allows CO_2 to still increase $F_{surf,667}$ in the (-) region.

Taking these effects into account, $F_{surf,667}$ in an atmosphere with H_2O is:

$$\begin{aligned} F_{surf,667} &= 2\Delta w ln(\frac{q}{q_i})[\pi B(\nu_0, Ts) - I_d(667cm^{-1})], \\ &= 21.2cm^{-1} ln(\frac{q}{q_i})[\pi B(667cm^{-1}, Ts) - I_d(667cm^{-1})], \end{aligned} \tag{17}$$

where $I_d(667cm^{-1}) = 1/2 \times (I_d(-) + I_d(+))$, and $I_d(-)$ and $I_d(+)$ are calculated by substituting Equations 11 and 12 into Equation 13. This expression quantifies how the presence of H_2O reduces $F_{surf,667}$ for a given change in CO_2. The difference between Equation 14 for a CO_2-only atmosphere and Equation 17 for a CO_2-H_2O atmosphere is given by the term 21.2 cm^{-1} $\ln(q/q_i)I_d(667cm^{-1})$ which describes the baseline downwelling flux from H_2O in the 667 cm^{-1} band. Using representative global-mean values of Ts = 280 K and RH = 0.75, this term equals 3.7 W/m^2, which should be compared to $F_{surf,667}$ = 5.5 W/m^2 for a CO_2-only atmosphere at the same conditions. H_2O thus significantly reduces the CO_2 surface forcing in the 667 cm^{-1} band, by about 67%.

The new bands overlap with the H_2O continuum, but since CO_2 emission is not saturated in this region and the continuum is relatively flat (the curvature in Figure 1 is exaggerated by the zoomed-in y-axis), their emission can still be approximated by two triangles. The optical thicknesses of H_2O and CO_2 are comparable in the new bands, so we must include both their contributions when computing I_d in the new bands:

$$\tau_d = \tau_d^{H_2O} + \tau_d^{CO_2}, \tag{18}$$

which can be evaluated using the expressions from Section 2. $F_{surf,new}$ is then obtained from Equation 15 as before, but now we evaluate I_d in Equation 13 using this combined value of τ_d. In addition, we assume the new bands have the same width w_{new} in a CO_2-H_2O as in CO_2-only atmosphere.

Putting things together, our analytical model for F_{surf} in a CO_2-H_2O atmosphere is:

$$\begin{aligned} F_{surf} = 21.2cm^{-1} ln(\frac{q}{q_i})[\pi B(667cm^{-1}, Ts) - I_d(667cm^{-1})] \\ +149.45cm^{-1}[I_d(new, q) - I_d(new, q_i)], \end{aligned} \tag{19}$$

where $I_d(667cm^{-1}) = 1/2 \times (I_d(-) + I_d(+))$ and $I_d(new, q) = \frac{1}{2}[I_d(L, q) + I_d(R, q)]$. Substituting Equations 10, 13, and 18 into Equation 19, using the Planck function at 667 cm^{-1} in place of the Planck functions for the (-) and (+) regions, and the Planck function at 1000 cm^{-1} in place of the Planck functions for the L and R new bands, and approximating with Taylor expansion gives:

$$\begin{aligned} F_{surf} &= 21.2cm^{-1} ln(2)\pi B(667cm^{-1}, Ts)e^{-\tau_d^{H_2O}(667cm^{-1})} \\ &\quad +74.7cm^{-1}\pi B(1000cm^{-1}, Ts) \times \\ &\quad (46.5q_i + 71.4q_i)e^{-\tau_d^{H_2O}(new)}, \end{aligned} \tag{20}$$

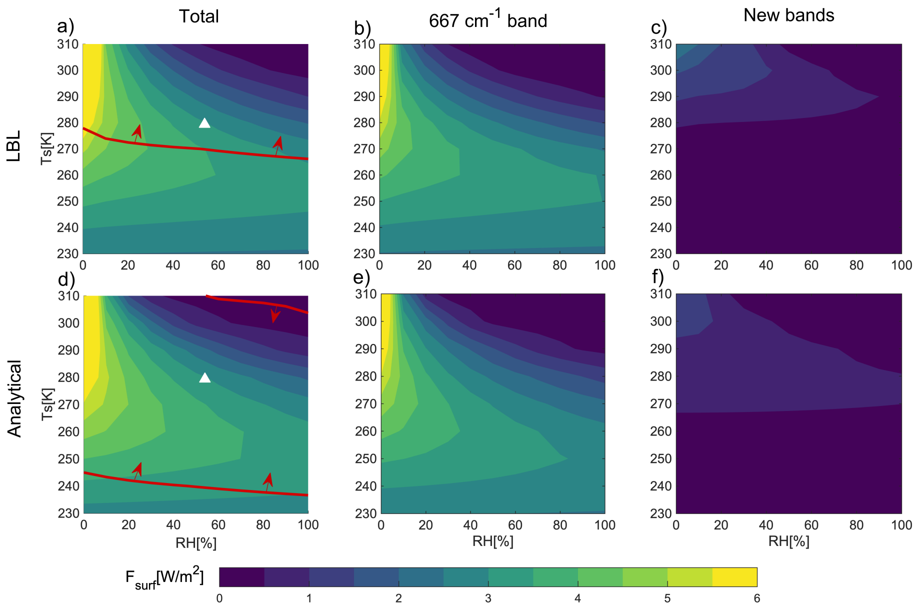

Figure 3. F_{surf} for Ts varying from 230 K to 310 K and RH varying from 0 to 100%, with CO_2 doubled from 280 ppm to 560 ppm. The top row shows the results of the LBL calculations and the bottom row shows the results of the analytical model. The left column shows the total forcing, the middle column shows the forcing due to the 667 cm^{-1} band and the right column shows the forcing due to the new bands. White triangles denote the global-mean Ts and RH of present-day Earth. The areas indicated by the red lines and arrows indicate conditions for which $F_{surf,new}$ accounts for more than 10% of the F_{surf}.

where $e^{-\tau_d^{H_2O}(667cm^{-1})} = (e^{-\tau_{d,rot}^{H_2O}(-)} + e^{-\tau_{d,ctn}^{H_2O}(+)})/2$, and $e^{-\tau_d^{H_2O}(new)} = (e^{-\tau_{d,ctn}^{H_2O}(L)} + e^{-\tau_{d,ctn}^{H_2O}(R)})/2$. F_{surf} increases with Ts due to both the 667 cm^{-1} and the new bands, decreases with $\tau_d^{H_2O}$ in both bands, and increases with CO_2 due to the CO_2-dependence of the optically thin new bands.

Comparing the analytical model with and without H_2O, as given by Equations 16 and 20, one can see that H_2O reduces F_{surf} by adding an attenuation factor of $e^{-\tau_d^{H_2O}}$. Our analytical model for F_{surf} is derived based on the difference in I_d. In Appendix S1.4, Equation A.8, we provide an alternative analytical model for F_{surf} analogous to the method used in Jeevanjee et al. (2021)'s model.

As an application of Equation 19, we calculate F_{surf} at the Amundsen-Scott South Pole Station (140.5°E, 89.5°S) under clear-sky conditions, using the following background state: (Ts, RH, CO_2, T_{tp}, Ps) = (245 K, 0.95, 380 ppm, 200 K, 10^5 Pa) and Γ = 6 K/km (Freese & Cronin, 2021). From Equation 19, we obtain F_{surf} = 3.45 W/m^2, consistent with the radiosonde-observed value of 3.33 W/m^2 (Loeb et al., 2018; Kato et al., 2018) and a value of 2.90 W/m^2 simulated using RRTMG (Freese & Cronin, 2021).

3.4 Validation against LBL model

We validate our analytical model for F_{surf} by comparing its estimates of F_{surf} for a CO_2-H_2O atmosphere with the results of our 1D LBL model. Figure 3 shows that our analytical model accurately captures the dependence of F_{surf} on RH and Ts (Figure 3a,d; correlation coefficient r=0.98), although it is more accurate in the 667 cm^{-1} band (r=0.99) than in the new bands (r=0.80). In the new bands, our model tends to underestimate $F_{surf,new}$ at Ts > 290 K and overestimate it at Ts < 290 K (see Figure S5). The bias of our analytical model in the new bands can be related to our imperfect parameterization of H_2O, which is likely further compounded by our approximation of the downwelling surface flux via Equation 13.

Both the LBL calculations and our analytical model show that F_{surf} increases with Ts in the CO_2-only case (i.e., when RH = 0), but is non-monotonic for RH values above ∼10%, and generally peaks at a relatively cold Ts of 250 – 270 K. The decrease in F_{surf} at higher Ts is due to the H_2O masking effect. As seen in the right panels of Figure 1, H_2O masks the emission from certain wavenumbers, and this masking strengthens as Ts increases and the water vapor path lengthens, counteracting the increase in F_{surf} due to the increase in $\pi B(\nu, Ts)$ as Ts rises. The latter effect only wins out at relatively low Ts and RH. Figure 3 also shows that F_{surf} is dominated by the 667 cm^{-1} band at low Ts while the new bands become dominant at high Ts and RH. For Ts > 290 K and RH > 50%, the new bands contribute over 50% of the total F_{surf} (see Figure S6).

3.5 Analytical model for F_{atm}

Finally, we combine our analytical model for F_{surf} with Jeevanjee et al. (2021)'s analytical model for F_{TOA} to develop an analytical model for F_{atm}. In doing so, we will ignore the contribution to F_{atm} from the new bands. The new bands were not included in Jeevanjee et al. (2021)'s model, though we find that these bands can substantially contribute to F_{atm} once Ts > 270 K (Figure S6). In Appendix S1 we derive an extension of Jeevanjee et al. (2021)'s F_{TOA} model which includes the effect of the new bands; for the rest of this paper, however, our discussion of F_{atm} is based on the simpler model which ignores the new bands.

For a CO_2-only atmosphere, combining the analytical model for F_{TOA} (Equation 14 in Jeevanjee et al. (2021)) and our analytical model for F_{surf} yields

$$F_{atm} = -21.2cm^{-1}ln\left(\frac{q}{q_i}\right)\pi B(667cm^{-1}, T_{tp}), \tag{21}$$

which depends only on T_{tp} and is independent of Ts (see Figure 4). For CO_2-only F_{atm} is always negative, so an increase in CO_2 always increases the atmosphere's radiative cooling (and increases precipitation).

For a CO_2-H_2O atmosphere we obtain:

$$\begin{aligned} F_{atm} &= 21.2cm^{-1}ln\left(\frac{q}{q_i}\right)[\pi B(667cm^{-1}, \overline{T_{em}}) - \pi B(667cm^{-1}, T_{tp}) - \\ &\quad \pi B(667cm^{-1}, Ts) + I_d(667cm^{-1})]. \end{aligned} \tag{22}$$

Where $\overline{T_{em}}$ = min(Ts, T_{em}), T_{em} is the effective emission temperature of H_2O, which depends quadratically on RH (Jeevanjee et al., 2021).

Plugging Equations 11, 12, and 13 into Equation 19 gives:

$$\begin{aligned} F_{atm} &= 21.2cm^{-1}ln(2)[\pi B(667cm^{-1}, \overline{T_{em}}) - \pi B(667cm^{-1}, T_{tp}) \\ &\quad -\pi B(667cm^{-1}, Ts)e^{-\tau_d^{H_2O}(667cm^{-1})}], \end{aligned} \tag{23}$$

where $e^{-\tau_d^{H_2O}(667cm^{-1})} = (e^{-\tau_{d,rot}^{H_2O}(-)} + e^{-\tau_{d,ctn}^{H_2O}(+)})/2$. F_{atm} is now a function of Ts, RH, and T_{tp}. In Appendix S1.4, we present an alternative model for calculating F_{surf} (Equation A.8) and F_{atm} (Equation A.9) using the same approach as in Jeevanjee et al. (2021), which employs an effective downward emission temperature T_{dem}. Equation A.9 provides an intuitive understanding of the dependencies of F_{atm} on H_2O, Ts, and T_{tp}:

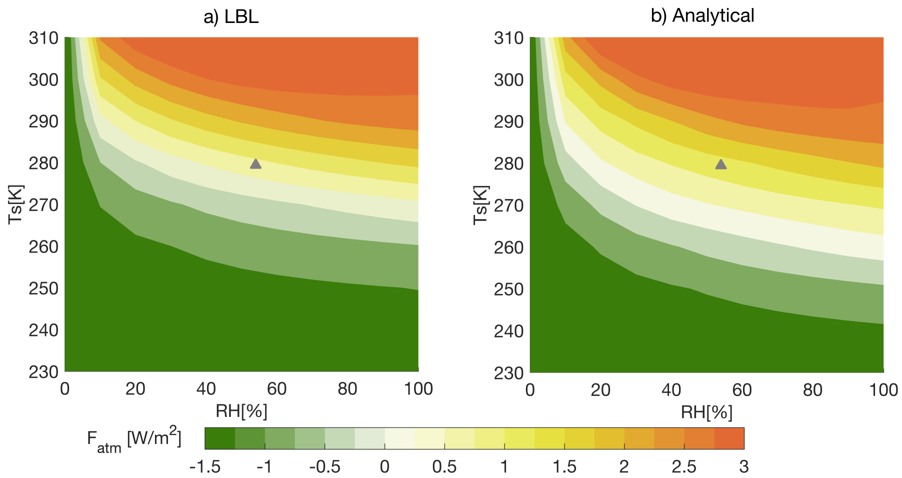

Figure 4. F_{atm} obtained from the LBL model (a) and our analytical model (b) for Ts ranging from 230 K to 310 K and RH from 0 to 100%, with CO_2 at 280 ppm. In the LBL model, F_{atm} is calculated using the entire CO_2 spectrum, whereas in the analytical model, F_{atm} only accounts for the 667 cm^{-1} band of CO_2. Triangles denote the global-mean Ts and RH of pre-industrial Earth from RFMIP.

as the H_2O concentration increases, T_{em} decreases, and T_{dem} increases, partially offsetting each other term's effect. Increases in Ts and decreases in T_{tp} enhance F_{atm} through the Planck function (see Figure 4).

In Figure 4 we validate the analytical model for F_{atm} (Equation 23) against the LBL model and present its state-dependence on Ts and RH. The analytical model for F_{atm} (Equation 23) reproduces the key features of the LBL calculations, though it tends to overestimate the forcing because it neglects the new bands. Neglecting the new bands has almost little impact on F_{TOA} at Ts $<$ 300 K, but leads the model to underestimate F_{surf}.

In contrast to a CO_2-only atmosphere, the sign of F_{atm} now varies depending on Ts and RH. At low Ts and RH, F_{atm} resembles the CO_2-only case and is negative. This means an increase in CO_2 increases the atmosphere's radiative cooling and increases precipitation. However, at high Ts and RH F_{atm} is positive. This means an increase in CO_2 reduces the atmosphere's radiative cooling and reduces precipitation. Interestingly, present-day global-mean conditions are surprisingly close to the boundary where F_{atm} flips sign. This suggests the CO_2-precipitation effect reverses sign in climates only moderately colder ($\sim$ 10 K) than today, while F_{atm} becomes significantly stronger in hot climates. This Ts-dependence is entirely due to the presence of H_2O, as F_{atm} becomes independent of Ts as RH $\to$ 0 (see the left sides of Figure 4a,b). H_2O thus crucially controls whether an increase in CO_2 allows the atmosphere to shed more energy (at low Ts and RH) or to retain more energy (at high Ts and RH).

4 Spatial Forcings and ΔP_{CO_2} in RFMIP

In this section we compare our analytical models for clear-sky longwave F_{surf} (Equation 19) and F_{atm} (Equation 23) with outputs from GCMs participating in RFMIP. We begin by evaluating global-mean F_{surf} and F_{atm} using GCM output. Subsequently, we use Equation 1 to compute ΔP_{CO_2} and its spatial distribution in RFMIP, and compare ΔP_{CO_2} as diagnosed from GCMs to ΔP_{CO_2} predicted by our analytical model for F_{atm}.

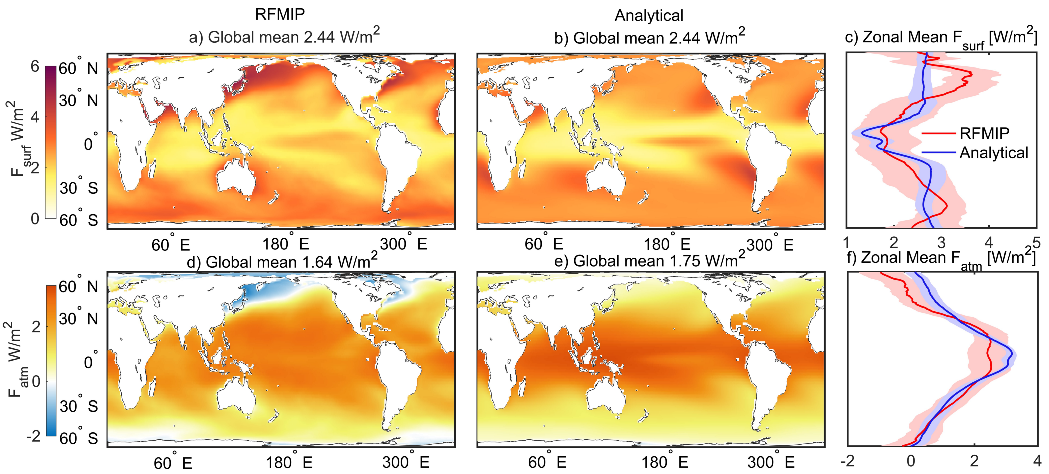

Figure 5. Top row: Multi-model mean RFMIP F_{surf} (left), the estimate from the analytical model (middle), and zonal means (right panel). The 95% confidence interval for the zonal mean is shaded. Bottom row: Same as top row but for F_{atm}.

4.1 RFMIP data

RFMIP is a subproject of CMIP6 designed for investigating uncertainties in radiative forcing (Pincus et al., 2016). The experiments used here comprise 'piClim-control' and 'piClim-4$\times CO_2$', both of which use fixed pre-industrial sea surface temperatures (SSTs) and sea-ice and were run for 30 years (Eyring et al., 2016). The piClim-control experiment represents a scenario with CO_2 at pre-industrial levels that serves as baseline for radiative forcing calculations. The piClim-4$\times CO_2$ experiment features quadrupled CO_2 concentrations compared to pre-industrial.

We compute F_{TOA} and F_{surf} by subtracting the relevant fields for piClim-control from piClim-4$\times CO_2$. It should be noted that land surface temperatures are not held constant in the RFMIP experiments. To ensure compatibility with the definition of forcing (change in flux while keeping temperature constant), we therefore restrict our analysis to ocean grid points in the RFMIP simulations.

We use data from 15 GCMs participating in RFMIP to evaluate the spatial patterns of F_{surf}, F_{atm}, and ΔP_{CO_2}. For each of these variables, we perform calculations separately under clear-sky and all-sky conditions. For comparison we then evaluate our analytical model at each latitude-longitude grid point separately. The inputs to our analytical model are Ts, T_{tp}, Γ, and RH, which we derive from RFMIP data as follows. For Ts, we use the atmospheric temperature at 850 hPa, which avoids complications in inversion regions. The tropopause temperature T_{tp} is defined as the temperature at a fixed pressure level that decreases linearly from 100 hPa at the equator to 300 hPa at the poles (Soden et al., 2008). Γ is taken as the vertically-averaged, pressure-weighted lapse rate. RH is the ratio of the vertically-averaged, pressure-weighted specific humidity to the vertically-averaged, pressure-weighted saturation specific humidity inside the troposphere. For all variables, we use multi-year averages of the pre-industrial values from each model to serve as inputs in our analytical model and calculate spatial patterns for each model individually.

4.2 Spatial patterns of $\mathbf{F}_{surf}$, $\mathbf{F}_{atm}$, and $\mathbf{\Delta P}_{CO_2}$

We use Equations 19 and 23 with input data from the piClim-control experiments to estimate the spatial distribution of F_{surf} and F_{atm} in RFMIP (Figure 5). For further diagnosis of any discrepancies between RFMIP models and our F_{atm} estimate, we also estimate F_{TOA} using Jeevanjee et al. (2021)'s analytical model (see Figure S11).

The analytical model for F_{surf} exactly matches the global-mean F_{surf} of 2.44 W/m^2 (Figure 5a,b), and produces good agreement with the zonal structure of F_{surf}, which is characterized by weaker values in the tropics and stronger values in the extratropics (Figure 5c). Comparing with our 1D results (Section 3) shows that the tropical minimum in F_{surf} is a result of high Ts and RH, in which H_2O masks CO_2 and thus diminishes F_{surf}.

The most significant discrepancies are in the temperate regions of the Northwest Pacific and Northwest Atlantic, where our model fails to capture the high values of F_{surf}. We find that these strong F_{surf} values are caused by local increases in RH after CO_2-doubling (Figure S12), which lead to increased downward longwave emission reaching the surface. Our analytical model assumes RH remains fixed during CO_2-doubling, so it cannot account for this effect.

The analytical model for F_{atm} also produces a good match to the RFMIP data. It estimates a global mean F_{atm} of 1.75 W/m^2, close to the RFMIP value of 1.64 W/m^2. The spatial patterns are also comparable; both RFMIP models and our analytical expressions show that F_{atm} is large in the deep tropics and becomes small at high latitudes. This pattern is consistent with our 1D results in Figure 4, which show that F_{atm} becomes small and even reverses sign at low Ts and low RH.

There are two primary differences between the analytic model estimates of F_{atm} and RFMIP results. First, the model does not capture the negative F_{atm} in the northwest Pacific and Atlantic, which is driven by the large F_{surf} there. Interestingly, these negative F_{atm} are compensated by relatively strong, positive F_{atm} over the eastern parts of the basin, leading to pronounced zonal asymmetries. Second, the analytical model predicts a narrow band of large F_{atm} over the equator, whereas the RFMIP data has a slightly weaker forcing maximum that is spread over a wider band of latitudes. A similar discrepancy is seen in the F_{TOA} comparison in Figure S11 and is likely due to our simplified estimate of tropopause pressures and temperatures (i.e., linearly decreasing from equator to pole).

We next evaluate the effectiveness of using our clear-sky longwave expressions for F_{atm} to predict ΔP_{CO_2} in RFMIP models. We do this by calculating the precipitation change in each RFMIP model, which is equal to ΔP_{CO_2}. We further use energy balance to decompose ΔP_{CO_2} into separate contributions due to changes in longwave, shortwave, and sensible heat fluxes under clear-sky conditions (Figure 6c). Interestingly, cloud radiative effects contribute only marginally to the total ΔP_{CO_2} in RFMIP (see Figure S13), so we do not further discuss cloud changes.

We begin by comparing the global-mean precipitation changes. Substituting the global-mean F_{atm} from RFMIP into Equation 1 gives:

$$\Delta P_{CO_2} = \frac{-F_{atm}}{L} = \frac{-1.64W/m^2}{2.5 \times 10^6 J/kg} = -0.057mm/day. \tag{24}$$

Similarly, our analytical model gives an estimate of $\sim$ -0.06 mm/day, or an overestimate of 5%. Despite the good agreement in the global-mean ΔP_{CO_2} between the analytical model and RFMIP data, changes in clear-sky longwave fluxes account for only 62% of total ΔP_{CO_2} in the ensemble-mean (see Table S3), with the rest coming from changes in clear-sky shortwave fluxes and, to a lesser extent, in sensible heat fluxes. In Figure 6b, the total ΔP_{CO_2} is 0.092 mm/day in RFMIP, and the pattern of ΔP_{CO_2} shows large meridional variations, with strong decreases in the Intertropical Convergence Zone(ITCZ) and

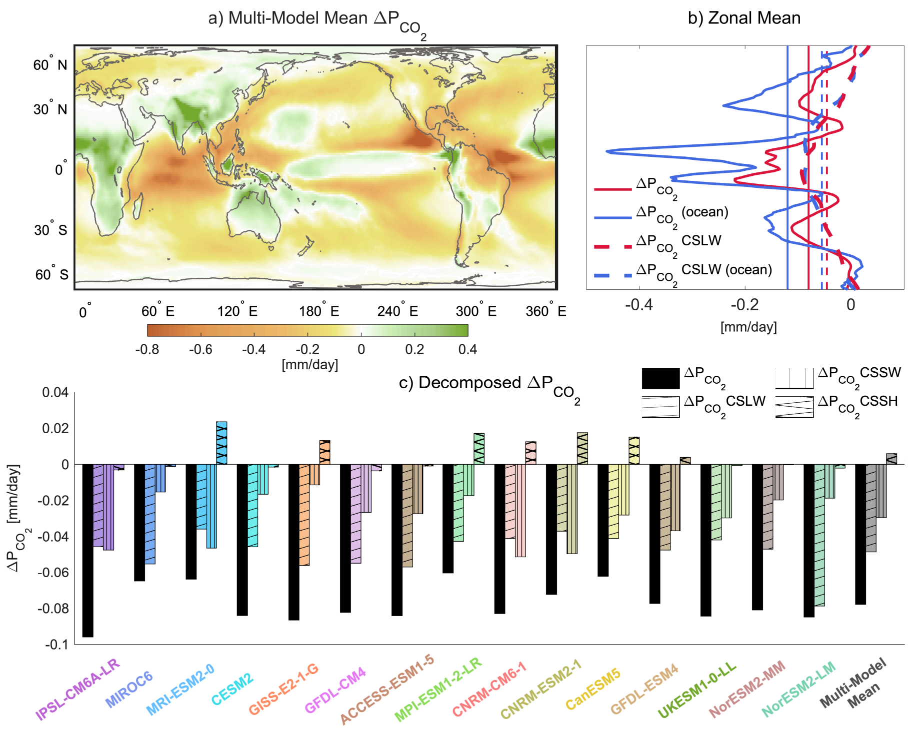

Figure 6. Changes in precipitation due to CO_2 doubling ΔP_{CO_2}. a) The multi-model mean precipitation change caused by CO_2 doubling in 15 RFMIP models (ΔP_{CO_2}). b) Zonal mean of ΔP_{CO_2} in a). The dashed curves show the zonal mean precipitation changes from the clear-sky longwave forcing F_{atm} (ΔP_{CO_2} CSLW). The red and blue dashed curves represent all points and ocean-only points, respectively. Straight lines are to the global-mean of the respective colored curves. c) The global-mean ΔP_{CO_2} simulated by each of the 15 RFMIP models and the multi-model mean (black bars), as well as the contributions from changes in clear-sky longwave radiation (CSLW), clear-sky shortwave radiation (CSSW), and the clear-sky sensible heat flux (CSSH) shown by colored bars.

over the mid-latitude storm tracks. In Figure 6a, we also show changes in precipitation over land, where precipitation increases over most locations except for Europe and western Asia, North America, and the Amazon.

The clear-sky shortwave radiative forcing arises due to changes in absorption by CO_2 and atmospheric water vapor. Both CO_2 and H_2O have shortwave absorption bands and increases in CO_2 drive increases in atmospheric temperatures, and thus in atmospheric water vapor levels. Consequently, even with fixed surface temperatures, higher levels of CO_2 lead to more shortwave absorption and a positive atmospheric shortwave forcing. Figure S12 compares ΔP_{CO_2} due to clear sky shortwave absorption (CSSW) with changes in specific humidity, showing that regions with substantial increases in H_2O correspond to areas experiencing significant reductions in ΔP_{CO_2} due to CSSW. However, even in regions where H_2O decreases, there is still a reduction in ΔP_{CO_2} due to CSSW via CO_2 shortwave absorption, which is higher near the equator and lower at the poles.

5 Discussion and Conclusion

The radiative forcing at the top-of-atmosphere (F_{TOA}) represents the increase in net incoming radiation to Earth per CO_2-doubling, whereas the radiative forcing at the surface (F_{surf}) represents the corresponding increase in radiation reaching the surface. The difference between F_{TOA} and F_{surf}, termed the radiative forcing of the atmosphere (F_{atm}), quantifies the increase in radiation retained within the atmosphere per CO_2-doubling. Because changes in atmospheric radiative cooling are closely linked to changes in latent heat fluxes and precipitation via energy balance, F_{atm} can thus be used to estimate the direct precipitation change per CO_2-doubling (ΔP_{CO_2}).

Accurate computation of these forcings requires simulations with comprehensive climate models and line-by-line radiative transfer codes, making it hard to fully discern the basic physics at play. In recent work, Jeevanjee et al. (2021) proposed an analytical model for clear-sky longwave (CSLW) F_{TOA}, offering insights into the factors controlling F_{TOA}. In this study, we have developed an analogous analytical model for CSLW F_{surf}. By combining this with the CSLW F_{TOA} model of Jeevanjee et al. (2021), our work yields an analytical model for CSLW F_{atm} and hence for ΔP_{CO_2}. We also extend Jeevanjee et al. (2021)'s model to include the new CO_2 bands at around 1000 cm^{-1}, providing a more comprehensive analytical model for F_{TOA} and F_{atm} in the Appendix S1.

Our analytical model for F_{surf} predicts that F_{surf} is a function of Ts, RH, Γ, and CO_2. Under present-day Earth climate conditions, F_{surf} generally decreases with increasing Ts, increasing RH, and decreasing Γ due to the masking effect of water vapor on changes in CO_2 longwave emission. F_{surf} increases with increasing CO_2 before CO_2 arrives $\sim 10^4$ ppm. The model successfully reproduces the global-mean F_{surf} of 2.44 W/m^2 in the RFMIP ensemble-mean ($\sim$60% of F_{TOA}) and is also able to capture the meridional distribution of F_{surf}, which is largest in the extratopics and smallest in the tropics.

Our analytical model for F_{atm}, derived by combining the F_{TOA} and F_{aurf} models, accurately predicts F_{atm} in the RFMIP ensemble-mean, although it slightly overestimates the global-mean F_{atm} of 1.64 W/m^2 by 0.11 W/m^2 (6.7%). F_{atm} exhibits the opposite pattern to F_{surf}, being largest at warmer surface temperature and higher relative humidities. The F_{TOA} model adds an additional dependence on tropopause temperature T_{tp}, causing F_{atm} to peak in the tropics, where the combination of a cold tropopause and warm surface amplifies F_{atm}.

The contribution of the new bands to these forcings is significant at high temperatures (Ts>270 K, see Figure S6). In Appendix S1, we provide analytical models for forcings from the new bands at TOA, $F_{TOA,new}$ (equation A.3) and within the atmosphere, $F_{atm,new}$ (equation A.5), extending Jeevanjee et al. (2021)'s F_{TOA} model, which only considers the 667 cm^{-1} band. We use this more comprehensive model to investigate F_{atm} state-dependence. Figure S9 shows F$_{atm}$ as a function of (Ts, RH), where F$_{atm,new}$ is almost always negative, except under conditions of extremely high Ts and RH. Figure S10 is F$_{atm}$ as a function of (Ts, CO_2) at RH = 0.75, while F$_{atm}$ calculated by merely equation 23 is independent of CO_2. In Figure S10, at CO_2 from 0 to 10^5 ppm, F$_{atm} > 0$ for Ts > 280 K, leading to a reduction in precipitation; F$_{atm} < 0$ for Ts < 280 K, resulting in an increase in precipitation. The larger the CO_2 concentration, the larger the magnitude of F$_{atm}$, amplifying the precipitation effects of CO_2-doubling.

Our model for F$_{atm}$ (Equation 23) accurately reproduces F$_{atm}$ in both LBL calculations and RFMIP. However, the longwave clearsky F$_{atm}$ explains only about two-thirds (62%) of the total CO_2-driven precipitation change ΔP$_{CO_2}$ in RFMIP models, while the remaining precipitation change is largely due to increases in atmospheric clear-sky shortwave absorption. Both CO_2 and H_2O absorb SW radiation, and the pattern of ΔP$_{CO_2}$ due to shortwave radiation is largely correlated with changes in specific humidity, with the largest decreases in precipitation seen in moist, tropical regions. Our study thus only provides a rough explanation for the precipitation change due to CO_2 changes; future research could refine this approach by focusing on the clearsky SW forcing from CO_2 and H_2.

Another limitation of our model is the assumption that RH is fixed before and after CO_2-doubling. Several regions do experience notable changes in RH, particularly the Atlantic and Pacific storm track regions, where increases in RH lead to larger F$_{surf}$ and smaller (negative) F$_{atm}$ than predicted by our model (Figure 5). Finally, while not discussed in detail here, explaining the spatial pattern of changes in precipitation requires accounting for changes in horizontal energy transport, though the global mean of the changes in horizontal energy transport is very small (Manabe & Wetherald, 1975). The local ΔP$_{CO_2}$ can be written as:

$$\Delta P_{CO_2} = \frac{-F_{atm} - \Delta SH + \Delta H}{L}, \tag{25}$$

where ΔSH denotes the change in upward sensible heat flux at the surface per CO_2-doubling; ΔH is the change in column-integrated dry static energy flux divergence, $\Delta H = \nabla\cdot\int u\, s\frac{dp}{g}$, where u is horizontal velocity, $s = CpT + gz$ is dry static energy, Cp is specific heat capacity of air, T is temperature, and g gravity acceleration (Muller & O'Gorman, 2011). Our analytical approach is sufficient to roughly capture the spatial pattern of F_{atm} in Equation 25; a similar understanding of the spatial patterns of ΔSH and ΔH would thus be sufficient to yield an understanding of the local change in latent heat fluxes ΔP_{CO_2}.

Despite these limitations, our analytical model for clear-sky longwave surface forcing performs well in tests against LBL calculations and RFMIP data. It provides detailed insight into the nature of CO_2's surface and atmospheric forcings, as well as a first insight into the direct response of precipitation to CO_2 changes. Our results thus allow one to reason about how F$_{surf}$ and F$_{atm}$ vary in space and across climate states, with implications for surface flux changes and the response of the hydrologic cycle to solar geoengineering. Our results can also be used to identify potential biases in climate model simulations of F$_{surf}$ and F$_{atm}$ by highlighting their dependencies on surface temperature, atmospheric humidity, lapse-rate, and tropopause temperatures.

References

Allen, M. R., & Ingram, W. J. (2002). Constraints on future changes in climate and the hydrologic cycle. *Nature*, *419*(6903), 224–232.

Andrews, T., & Forster, P. M. (2010). The transient response of global-mean precipitation to increasing carbon dioxide levels. *Environmental Research Letters*, *5*(2), 025212.

Andrews, T., Forster, P. M., Boucher, O., Bellouin, N., & Jones, A. (2010). Precipitation, radiative forcing and global temperature change. *Geophysical research letters*, *37*(14).

Bala, G., Duffy, P., & Taylor, K. (2008). Impact of geoengineering schemes on the global hydrological cycle. *Proceedings of the National Academy of Sciences*, *105*(22), 7664–7669.

Chen, Y.-T., Huang, Y., & Merlis, T. M. (2023). The global patterns of instantaneous co 2 forcing at the top-of-atmosphere and surface. *Journal of Climate*, 1–37.

Douville, H., Raghavan, K., Renwick, J., Allan, R. P., Arias, P. A., Barlow, M., ... others (2021). Water cycle changes.

Etminan, M., Myhre, G., Highwood, E. J., & Shine, K. P. (2016). Radiative forcing of carbon dioxide, methane, and nitrous oxide: A significant revision of the methane radiative forcing. *Geophysical Research Letters*, *43*(24), 12–614.

Eyring, V., Bony, S., Meehl, G. A., Senior, C. A., Stevens, B., Stouffer, R. J., & Taylor, K. E. (2016). Overview of the coupled model intercomparison project phase 6 (cmip6) experimental design and organization. *Geoscientific Model Development*, *9*(5), 1937–1958.

Fehr, S. M., & Krossing, I. (2020). Spectroscopic signatures of pressurized carbon dioxide in diffuse reflectance infrared spectroscopy of heterogeneous catalysts. *ChemCatChem*, *12*(9), 2622–2629.

Freese, L. M., & Cronin, T. W. (2021). Antarctic radiative and temperature responses to a doubling of co2. *Geophysical Research Letters*, *48*(17), e2021GL093676.

Gordon, I. E., Rothman, L. S., Hill, C., Kochanov, R. V., Tan, Y., Bernath, P. F., ... others (2017). The hitran2016 molecular spectroscopic database. *Journal of quantitative spectroscopy and radiative transfer*, *203*, 3–69.

Hartmann, D. L., & Larson, K. (2002). An important constraint on tropical cloud-climate feedback. *Geophysical research letters*, *29*(20), 12–1.

Jeevanjee, N., & Fueglistaler, S. (2020). Simple spectral models for atmospheric radiative cooling. *Journal of the Atmospheric Sciences*, *77*(2), 479–497.

Jeevanjee, N., & Romps, D. M. (2018). Mean precipitation change from a deepening troposphere. *Proceedings of the National Academy of Sciences*, *115*(45), 11465–11470.

Jeevanjee, N., Seeley, J. T., Paynter, D., & Fueglistaler, S. (2021). An analytical model for spatially varying clear-sky co 2 forcing. *Journal of Climate*, *34*(23), 9463–9480.

Kato, S., Rose, F. G., Rutan, D. A., Thorsen, T. J., Loeb, N. G., Doelling, D. R., ... Ham, S.-H. (2018). Surface irradiances of edition 4.0 clouds and the earth's radiant energy system (ceres) energy balanced and filled (ebaf) data product. *Journal of Climate*, *31*(11), 4501–4527.

Koll, D. D., & Cronin, T. W. (2018). Earth's outgoing longwave radiation linear due to h2o greenhouse effect. *Proceedings of the National Academy of Sciences*, *115*(41), 10293–10298.

Koll, D. D., & Cronin, T. W. (2019). PyRADS: Python Radiation Model for Planetary Atmospheres. *Astrophysics Source Code Library*, ascl–1908.

Koll, D. D., Jeevanjee, N., & Lutsko, N. J. (2023). An analytic model for the clear-sky longwave feedback. *Journal of the Atmospheric Sciences*.

Kvalevåg, M. M., Samset, B. H., & Myhre, G. (2013). Hydrological sensitivity to greenhouse gases and aerosols in a global climate model. *Geophysical Research Letters*, *40*(7), 1432–1438.

Liu, J., Yang, J., Ding, F., Chen, G., & Hu, Y. (2024). Hydrologic cycle weakening in hothouse climates. *Science Advances*, *10*(17), eado2515.

Loeb, N. G., Doelling, D. R., Wang, H., Su, W., Nguyen, C., Corbett, J. G., ... Kato, S. (2018). Clouds and the earth's radiant energy system (ceres) energy balanced and filled (ebaf) top-of-atmosphere (toa) edition-4.0 data product. *Journal of climate*, *31*(2), 895–918.

Manabe, S., & Wetherald, R. T. (1975). The effects of doubling the co 2 concentration on the climate of a general circulation model. *Journal of Atmospheric Sciences*, *32*(1), 3–15.

Mlawer, E. J., Payne, V. H., Moncet, J.-L., Delamere, J. S., Alvarado, M. J., & Tobin, D. C. (2012). Development and recent evaluation of the mt_ckd model of continuum absorption. *Philosophical Transactions of the Royal Society A: Mathematical, Physical and Engineering Sciences*, *370*(1968), 2520–2556.

Muller, C. J., & O'Gorman, P. (2011). An energetic perspective on the regional response of precipitation to climate change. *Nature Climate Change*, *1*(5), 266–271.

Myhre, G., Forster, P., Samset, B., Hodnebrog, Ø., Sillmann, J., Aalbergsjø, S., ... others (2017). Pdrmip: A precipitation driver and response model intercomparison project—protocol and preliminary results. *Bulletin of the American Meteorological Society*, *98*(6), 1185–1198.

O'Gorman, P. A., & Schneider, T. (2008). The hydrological cycle over a wide range of climates simulated with an idealized gcm. *Journal of Climate*, *21*(15), 3815–3832.

Pendergrass, A. G., & Hartmann, D. L. (2014). Changes in the distribution of rain frequency and intensity in response to global warming. *Journal of Climate*, *27*(22), 8372–8383.

Pierrehumbert, R. T. (2002). The hydrologic cycle in deep-time climate problems. *Nature*, *419*(6903), 191–198.

Pierrehumbert, R. T. (2010). *Principles of planetary climate*. Cambridge University Press.

Pincus, R., Forster, P. M., & Stevens, B. (2016). The radiative forcing model intercomparison project (rfmip): experimental protocol for cmip6. *Geoscientific Model Development*, *9*(9), 3447–3460.

Richardson, T., Samset, B., Andrews, T., Myhre, G., & Forster, P. (2016). An assessment of precipitation adjustment and feedback computation methods. *Journal of Geophysical Research: Atmospheres*, *121*(19), 11–608.

Ricke, K., Wan, J. S., Saenger, M., & Lutsko, N. J. (2023). Hydrological consequences of solar geoengineering. *Annual review of earth and planetary sciences*, *51*(1), 447–470.

Ricke, K. L., Morgan, M. G., & Allen, M. R. (2010). Regional climate response to solar-radiation management. *Nature Geoscience*, *3*(8), 537–541.

Romps, D. M. (2016). Clausius–clapeyron scaling of cape from analytical solutions to rce. *Journal of the Atmospheric Sciences*, *73*(9), 3719–3737.

Romps, D. M., Seeley, J. T., & Edman, J. P. (2022). Why the forcing from carbon dioxide scales as the logarithm of its concentration. *Journal of Climate*, *35*(13), 4027–4047.

Seeley, J. T., Lutsko, N. J., & Keith, D. W. (2021). Designing a radiative antidote to co2. *Geophysical Research Letters*, *48*(1), e2020GL090876.

Siler, N., Roe, G. H., Armour, K. C., & Feldl, N. (2019). Revisiting the surface-energy-flux perspective on the sensitivity of global precipitation to climate change. *Climate Dynamics*, *52*, 3983–3995.

Soden, B. J., Held, I. M., Colman, R., Shell, K. M., Kiehl, J. T., & Shields, C. A. (2008). Quantifying climate feedbacks using radiative kernels. *Journal of Climate*, *21*(14), 3504–3520.

Stephens, G. L., Li, J., Wild, M., Clayson, C. A., Loeb, N., Kato, S., ... Andrews, T. (2012). An update on earth's energy balance in light of the latest global observations. *Nature Geoscience*, *5*(10), 691–696.

Stevens, B., & Kluft, L. (2023). A colorful look at climate sensitivity. *Atmospheric Chemistry and Physics*, *23*(23), 14673–14689.

Acknowledgments

This section is optional. Include any Acknowledgments here. The acknowledgments should list:

All funding sources related to this work from all authors

Any real or perceived financial conflicts of interest for any author

Other affiliations for any author that may be perceived as having a conflict of interest with respect to the results of this paper.

It is also the appropriate place to thank colleagues and other contributors. AGU does not normally allow dedications.

Supporting Information for “An analytical model”

Yue Xu[1,2], Daniel D. B. Koll[1], Nicholas J. Lutsko[2]

[1]Laboratory for Climate and Ocean-Atmosphere Studies, Department of Atmospheric and Oceanic Sciences, Peking University, Beijing, People's Republic of China

[2]Scripps Institution of Oceanography, University of California, San Diego, La Jolla, California, USA

1. A Supplement of New Bands to F_{TOA}&F_{atm}

1.1. Upward radiative flux at TOA(I)from the new bands

In the context of present Earth's climate, the contribution of CO_2's new bands to F_{TOA} is minimal when compared to the 667 cm^{-1} band. However, the contribution of the new bands to F_{atm} becomes comparable to that of the 667 cm^{-1} band under both high-temperature, low-RH conditions and low-temperature, high-RH conditions(S6). Jeevanjee, Seeley, Paynter, and Fueglistaler (2021)'s F_{TOA} model reasonably omits CO_2's new bands, as their impact on F_{TOA} is negligible, only reaching approximately 20% under conditions of high temperature and RH. In this study, we present a preliminary analytical model to estimate the contributions of the new bands to both F_{TOA} and F_{atm}.

Following the same derivation approach as for I_d, we employ Beer's law and $\overline{T_{em}}$ from Jeevanjee et al. (2021)'s model, assuming I = 0 at the surface and determined by the optical thickness of H_2O τ^{H_2O} and CO_2 τ^{CO_2} at TOA. The magnitude of τ equals to τ_d given in the main text. $\overline{T_{em}}$ is described in the main text as $\overline{T_{em}} = \min(T_s, T_{em})$. T_{em} is emission temperature of H_2O. When $\tau^{CO_2} \ll 1$, I = $\pi B(\nu, \overline{T_{em}})$, and when $\tau^{CO_2} \gg 1$, I = $\pi B(\nu, T_{tp})$. For any τ^{CO_2}, we have I:

$$I = \pi B(\nu, T_{tp}) + [\pi B(\nu, \overline{T_{em}}) - \pi B(\nu, T_{tp})]exp(-\tau^{CO_2}), \tag{A.1}$$

As τ^{CO_2} increases, I decreases. When τ^{CO_2} or $\tau^{H_2O} = 1$ reaches the stratosphere, I arrives its minimum value $\pi B(\nu, T_{tp})$.

1.2. Derivation and Verification of the Analytical models for $\mathbf{F}_{\boldsymbol{TOA,new}}$

We apply the same methodology used in the main text to estimate $F_{surf,new}$ to derive $F_{TOA,new}$. We approximate the radiative flux of the new bands, I, using two triangles (see figure S7).

For CO_2-only case (see Figure S6 a&c), similar to Eq. 15, we obtain:

$$\begin{aligned} F_{TOA,new} &= \frac{1}{4} w_{TOA,new}[I(RS, q_i) - I(RS, q) + I(PQ, q_i) - I(PQ, q)] \\ &= \frac{1}{2} w_{TOA,new}[I(new, q_i) - I(new, q)] \\ &= 84.4[I(new, q_i) - I(new, q)] \\ &= 84.4[\pi B(new, T_s) - \pi B(new, T_{tp})] * [exp(-\tau^{CO_2}(q_i)) - exp(-\tau^{CO_2}(q))] \\ &= 84.4[\pi B(new, T_s) - \pi B(new, T_{tp})] * [exp(-\tau^{CO_2}(q_i)) - exp(-2\tau^{CO_2}(q))] \end{aligned} \tag{A.2}$$

Here, $w_{TOA,new} = 168.79$ cm^{-1} is fitted using the same method described in the main text for w_{new}.

For CO_2+H_2O case (see Figure S6 b&c), unlike the CO_2-only case, the optical depth submitted into Eq. A.1 is given by $\tau = \tau_{CO_2} + \tau_{H_2O}$, as Eq. 19.

$$\begin{aligned} F_{TOA,new} &= 84.4[I(new, q_i) - I(new, q)] \\ &= 84.4[\pi B(new, \overline{T_{em}}) - \pi B(new, T_{tp})] * [exp(-\tau^{CO_2}(q_i) - exp(-\tau^{CO_2}(q))] \\ &= 84.4[\pi B(new, \overline{T_{em}}) - \pi B(new, T_{tp})] * [exp(-\tau^{CO_2}(q_i) - exp(-2\tau^{CO_2}(q_i))]. \end{aligned} \tag{A.3}$$

F_{TOA} is determined by the difference in the Planck function at $\overline{T_{em}}$ and T_{tp}. The influence of CO_2 concentration is such that the doubling of higher concentrations result in a smaller increase in $F_{TOA,new}$. The presence of H_2O further reduces $F_{TOA,new}$.

Following Figure 3, we compare the results of the analytical model with those from LBL simulations (Figure S7). Overall, the analytical model reproduces the dependence of $F_{TOA,new}$ on RH and T_s: as temperature increases, $F_{TOA,new}$ rises, while at low temperatures, $F_{TOA,new}$ remains nearly independent of RH. When the T_s exceeds 290 K, higher RH leads to weaker $F_{TOA,new}$. This is because increased optical thickness of H_2O closes H_2O window at 290 K, which overwhelm CO_2.

1.3. Derivation and Verification of the Analytical models for $F_{atm,new}$

By combining the analytical model for $F_{TOA,new}$ with the analytical model for $F_{surf,new}$ presented in the main text, we derive an analytical model for $F_{atm,new}$.

For CO_2-only case, combining Eq. 15 and Eq. A.2, we have

$$
\begin{aligned}
F_{atm,new} &= 84.4[I(new,q_i) - I(new,q)] - 149.45[I_d(new,q) - I_d(new,q_i)] \\
&= 84.4[\pi B(new,T_s) - \pi B(new,T_{tp})] * [exp(-\tau^{CO_2}(q_i)) - exp(-\tau^{CO_2}(q))] \\
&- 149.45\pi B(new,T_s)[exp(-\tau^{CO_2}(q_i)) - exp(-\tau^{CO_2}(q))] \\
&= [-65.05\pi B(new,T_s) - 84.4\pi B(new,T_{tp})] * [exp(-\tau^{CO_2}(q_i)) - exp(-2\tau^{CO_2}(q_i))].
\end{aligned} \tag{A.4}
$$

For CO_2+H_2O case, combining Eq. 20 and Eq. A.3, we have

$$
\begin{aligned}
F_{atm,new} &= 84.4[I(new,q_i) - I(new,q)] - 149.45[I_d(new,q) - I_d(new,q_i)] \\
&= 84.4[\pi B(new,\overline{T_{em}}) - \pi B(new,T_{tp})] * [exp(-\tau^{CO_2}(q_i)) - exp(-\tau^{CO_2}(q))] \\
&- 149.45\pi B(new,T_s)exp(-\tau^{H_2O})[exp(-\tau^{CO_2}(q_i)) - exp(-\tau^{CO_2}(q))] \\
&= \{84.4[\pi B(new,\overline{T_{em}}) - \pi B(new,T_{tp})] - 149.45\pi B(new,T_s)exp(-\tau^{H_2O})\} \\
&* [exp(-\tau^{CO_2}(q_i)) - exp(-2\tau^{CO_2}(q_i))].
\end{aligned} \tag{A.5}
$$

Similar to F_{TOA}, the influencing factors are nearly identical, except for that an increase in either T_s or T_{tp} leads to a corresponding increase in F_{atm}. The doubling of CO_2 from higher concentrations results in a smaller increase in $F_{TOA,new}$. The presence of H_2O further reduces $F_{TOA,new}$ by $84.4\pi(B(new,T_s) - B(new,T_{em}))$.

As a verification to LBL model(Figure S8 c&f), Our model consistently calculates a negative $F_{atm,new}$, indicating that CO_2 doubling results in a reduction of energy retained in the atmosphere. In contrast, the LBL results show that under conditions of high temperature and humidity, increasing CO_2 leads to a positive $F_{atm,new}$. Figure S8 is identical to Figure 4, but with the addition of $F_{atm,new}$ and serves as a validation against the LBL model.

1.4. An Alternative Approach to Calculate F_{surf} – via $\overline{T_{dem}}$

Jeevanjee et al. (2021) calculates radiative flux by determining the emission temperature $\overline{T_{em}}$ from the optical thickness τ and then using the Planck function at $\overline{T_{em}}$ as the radiative flux. Radiative forcing is then derived from changes in this radiative flux before and after CO_2-doubling. In the main text, we provide a method for directly estimating the downward radiative flux from the optical thickness to compute surface radiative forcing. To maintain consistency in this comprehensive analytical model, we also present an alternative approach to calculate F_{surf} and F_{atm}, based on Jeevanjee et al. (2021)'s method —calculating the downward emission temperature $\overline{T_{dem}}$ from the downward optical thickness τ_d, using the Planck function at $\overline{T_{dem}}$ as the downward radiative flux I_d, and then deriving radiative forcing from the change in I_d. In the new bands, accurate calculations require considering the combined τ of both H_2O and CO_2. However, the relationship between τ and T is not readily solvable in this case. Therefore, we present calculations only for the 667 cm^{-1} band. Future studies could explore converting τ^{CO_2} into a function of T based on pressure-temperature relationships, and derive the inverse function of $\tau^{CO_2} + \tau^{H_2O}$ with respect to T using Mathematica.

Here, we employ a equivalent optical thickness τ_{eq} to calculate $\overline{T_{dem}}$. Jeevanjee et al. (2021) provided a formula for calculating the temperature at any given τ of H_2O. $\overline{T_{dem}}$ is the temperature at the downward emission optical thickness $\tau_{dem} = 1$.

τ_{dem} is equivalent to the optical thickness at τ_{eq}

$$\tau_{eq} = \tau^{H_2O} - \tau_{dem}. \tag{A.6}$$

The column optical thickness of H_2O τ^{H_2O} is given by Equations 11&12 (the column optical thickness is fixed no matter it is integrated from the bottom up or the top down).

Thus, by substituting Equation A.6 into Jeevanjee et al. (2021)'s Equations 9&12&13, we get that $\overline{T_{dem}}$ at $\tau_{dem} = 1$.

Then, the alternative way to calculate downward radiative flux I_d as shown in Equation 13 in the main text is:

$$I_d = \pi B(667cm^{-1}, \overline{T_{dem}}). \tag{A.7}$$

By substituting Equation A.7 back into Equation 18, we obtain the alternative way to calculate F_{surf}:

$$F_{surf} = 21.2cm^{-1}ln(\frac{q}{q_i})[\pi B(667cm^{-1}, Ts) - \pi B(667cm^{-1}, \overline{T_{dem}})]. \tag{A.8}$$

By substituting into Equation 23, we obtain the alternative way to calculate F_{atm}:

$$F_{atm} = 21.2cm^{-1}ln\left(\frac{q}{q_i}\right)[\pi B(667cm^{-1}, \overline{T_{em}}) - \pi B(667cm^{-1}, T_{tp}) - \\ \pi B(667cm^{-1}, Ts) + \pi B(667cm^{-1}, \overline{T_{dem}}]. \tag{A.9}$$

References

Jeevanjee, N., Seeley, J. T., Paynter, D., & Fueglistaler, S. (2021). An analytical model for spatially varying clear-sky co 2 forcing. *Journal of Climate*, *34*(23), 9463–9480.

The parameters used in this paper are listed in Table S1

Table S1. Parameters used in the analytical model of CO_2 F_{surf}

Parameter	Value	Description
l_{667}	10.6 cm^{-1}	spectroscopic decay parameter of 667 cm^{-1} band
w_{new}	298.9 cm^{-1}	width of new bands
$(-)$	550-600 cm^{-1}	wavenumbers at the left of 667 cm^{-1} band
$(+)$	750-800 cm^{-1}	wavenumbers at the right of 667 cm^{-1} band
ν_0	667 cm^{-1}	wavenumber at the center of 667 cm^{-1} band
ν_{RS}	960 cm^{-1}	wavenumber at the center of RS band
ν_{PQ}	1060 cm^{-1}	wavenumber at the center of PQ band
$(T_{ref}^{CO_2}, P_{ref}^{CO_2})$	(250 K, 100 hPa)	Reference T and P for CO_2 absorption coefficient
$(T_{ref}^{-,H_2O}, P_{ref}^{-,H_2O})$	(245 K, 370 hPa)	Reference T and P for H_2O absorption coefficient at left side of 667 cm^{-1} band (-)
$(T_{ref}^{+,H_2O}, P_{ref}^{+,H_2O})$	(275 K, 650 hPa)	Reference T and P for H_2O absorption coefficient at right side of 667 cm^{-1} band (+)
$(T_{ref}^{new,H_2O}, P_{ref}^{new,H_2O})$	(275 K, 650 hPa)	Reference T and P for H_2O absorption coefficient at new bands
RH_{ref}	0.75	Reference RH for H_2O absorption coefficient at right side of 667 cm^{-1} band (+) and new bands
κ_{ref}^{RS,CO_2}	$9.12{*}10^{-4}$ m^2kg^{-1}	Reference CO_2 absorption coefficient at the center of RS band
κ_{ref}^{PQ,CO_2}	1.40×10^{-3} m^2kg^{-1}	Reference CO_2 absorption coefficient at the center of PQ band
κ_{ref}^{-,H_2O}	1.50×10^{-1} m^2kg^{-1}	Reference H_2O absorption coefficient at left side of 667 cm^{-1} band (-)
κ_{ref}^{+,H_2O}	5.5×10^{-2} m^2kg^{-1}	Reference H_2O absorption coefficient at right side of 667 cm^{-1} band (+)
κ_{ref}^{RS,H_2O}	1.36×10^{-2} m^2kg^{-1}	Reference H_2O absorption coefficient at the center of RS band
κ_{ref}^{PQ,H_2O}	1.76×10^{-2} m^2kg^{-1}	Reference H_2O absorption coefficient at the center of PQ band

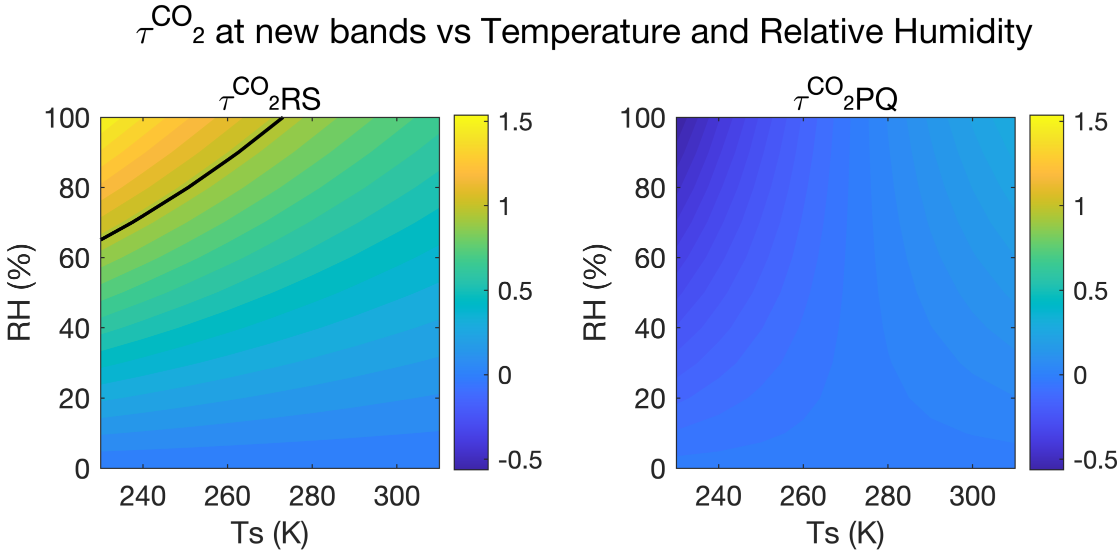

Figure S1. The optical thicknesses of the new CO_2 bands calculated from Equation 10 are shown as functions of Ts and RH at CO_2 = 1000 ppm. The left panel represents the RS band, and the right panel represents the PQ band. τ^{CO_2} for both bands is less than 1 in almost all conditions, while the optical thickness of 667 cm^{-1} band only reaches $\leq$1 at the boundaries

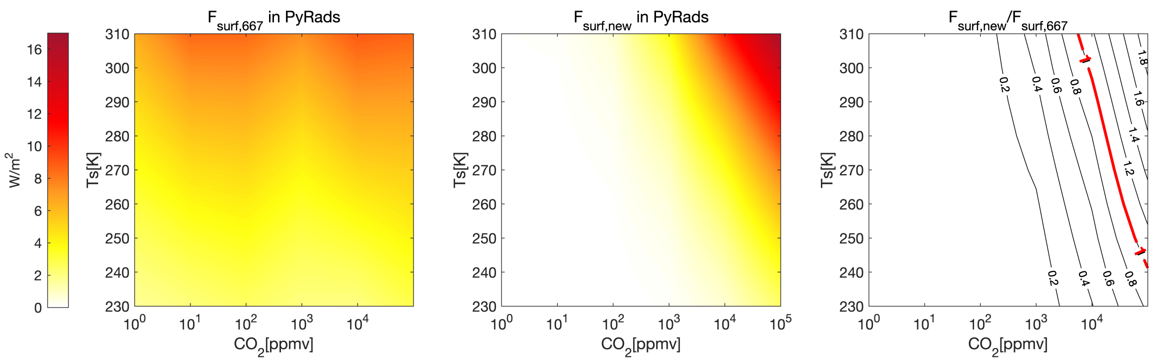

Figure S2. Under the CO_2-only scenario, $F_{surf,667}$ and $F_{surf,new}$, as well as the ratio $F_{surf,new}/F_{surf,667}$, are analyzed as functions of Ts and CO_2. The results illustrate under what conditions the new bands become more significant than the 667 band for CO_2-only induced F_{surf}.

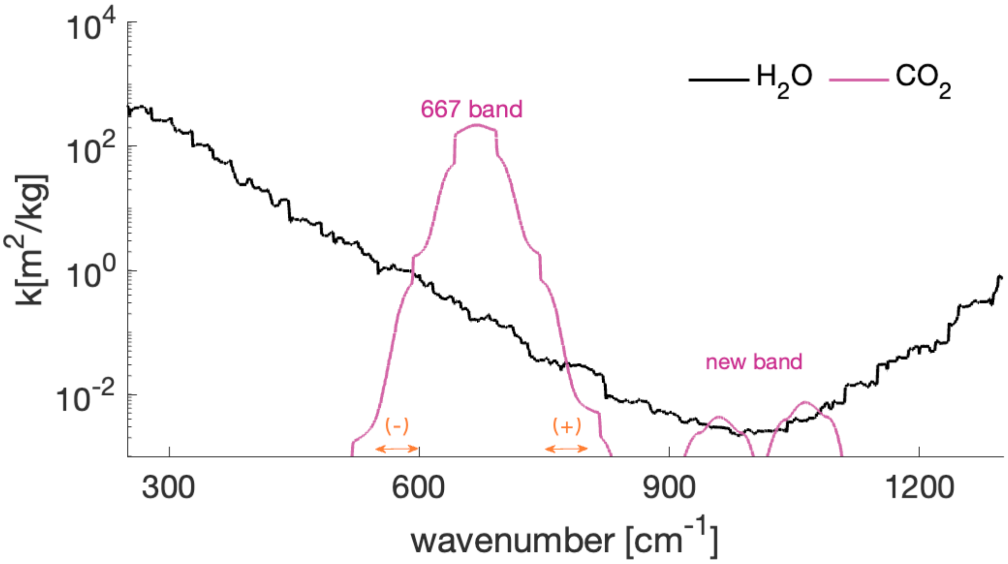

Figure S3. Absorption coefficients of H_2O and CO_2 at 500 hPa and 250 K. 667 cm^{-1} band and new bands of CO_2, (-) and (+) region are illustrated.

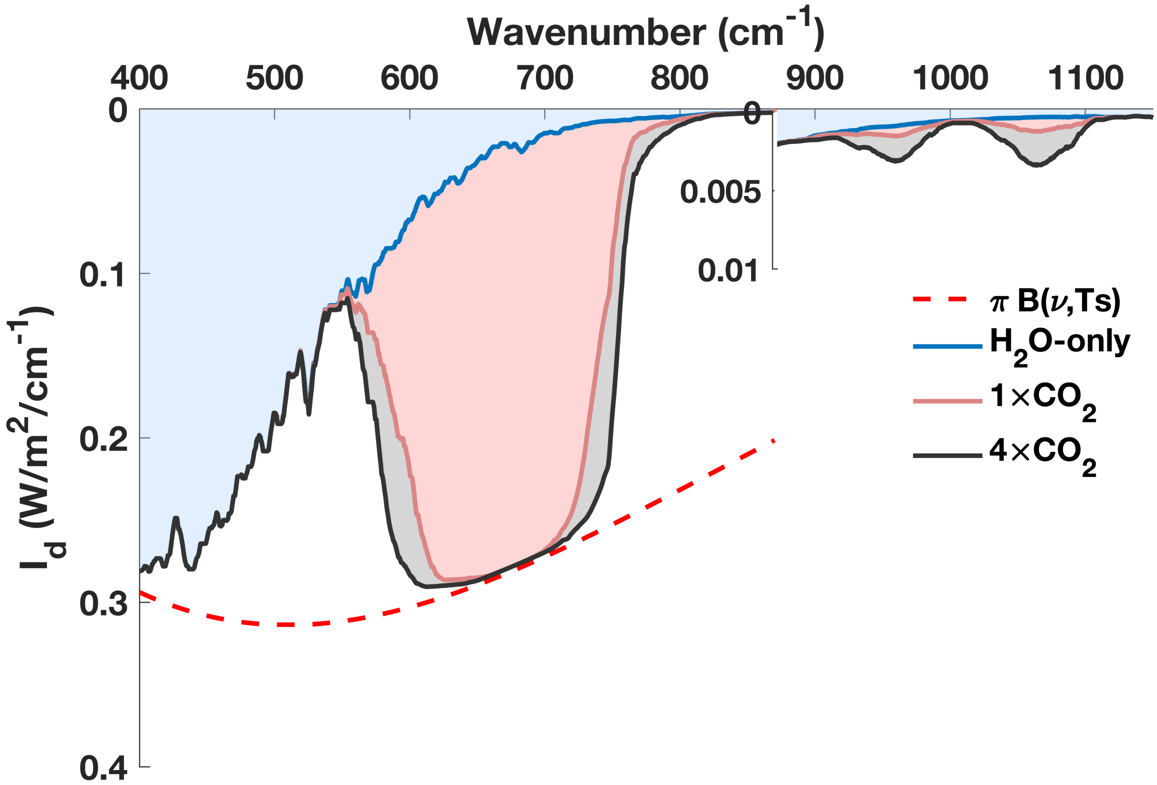

Figure S4. The downward radiative flux into the surface, I_d from a LBL model at CO_2 = 280 ppm (q_i) and 1120 ppm ($4q_i$) with Ts = 260 K and RH=0.75. The added blue curve represents I_d in the presence of H_2O-only, serving as an indicator of the background radiation that CO_2 replaces. Spectra are smoothed using a 50cm^{-1} sliding window. The x-axis is split at 870cm^{-1} to illustrate the 667 cm^{-1} band and the new band s of CO_2, with y-axis magnified by a factor of 10 at 870cm^{-1}.

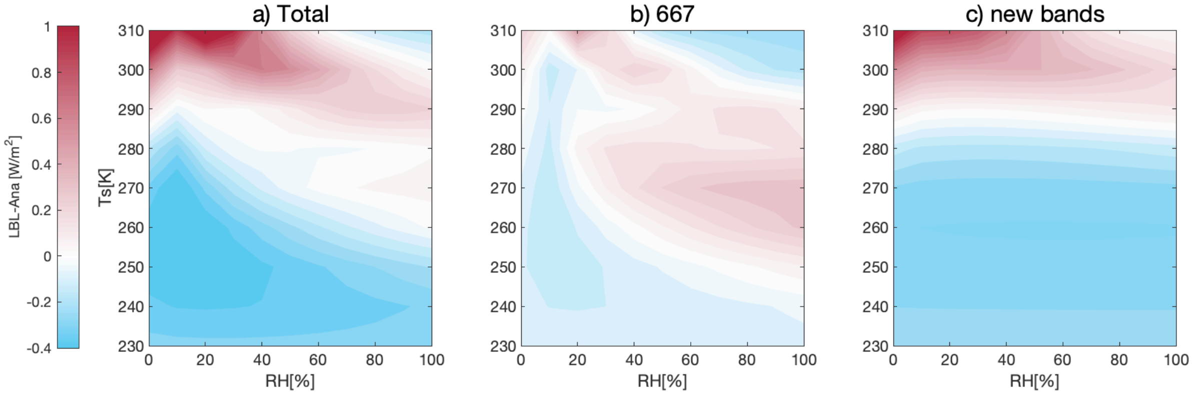

Figure S5. This figure shows the difference in F_{surf} between the LBL calculation results and our analytical model(LBL-Analytical) in Figure 3. From left to right, the plots correspond to the 667 cm^{-1} band + the new bands, the 667 cm^{-1} band, and the new bands, respectively.

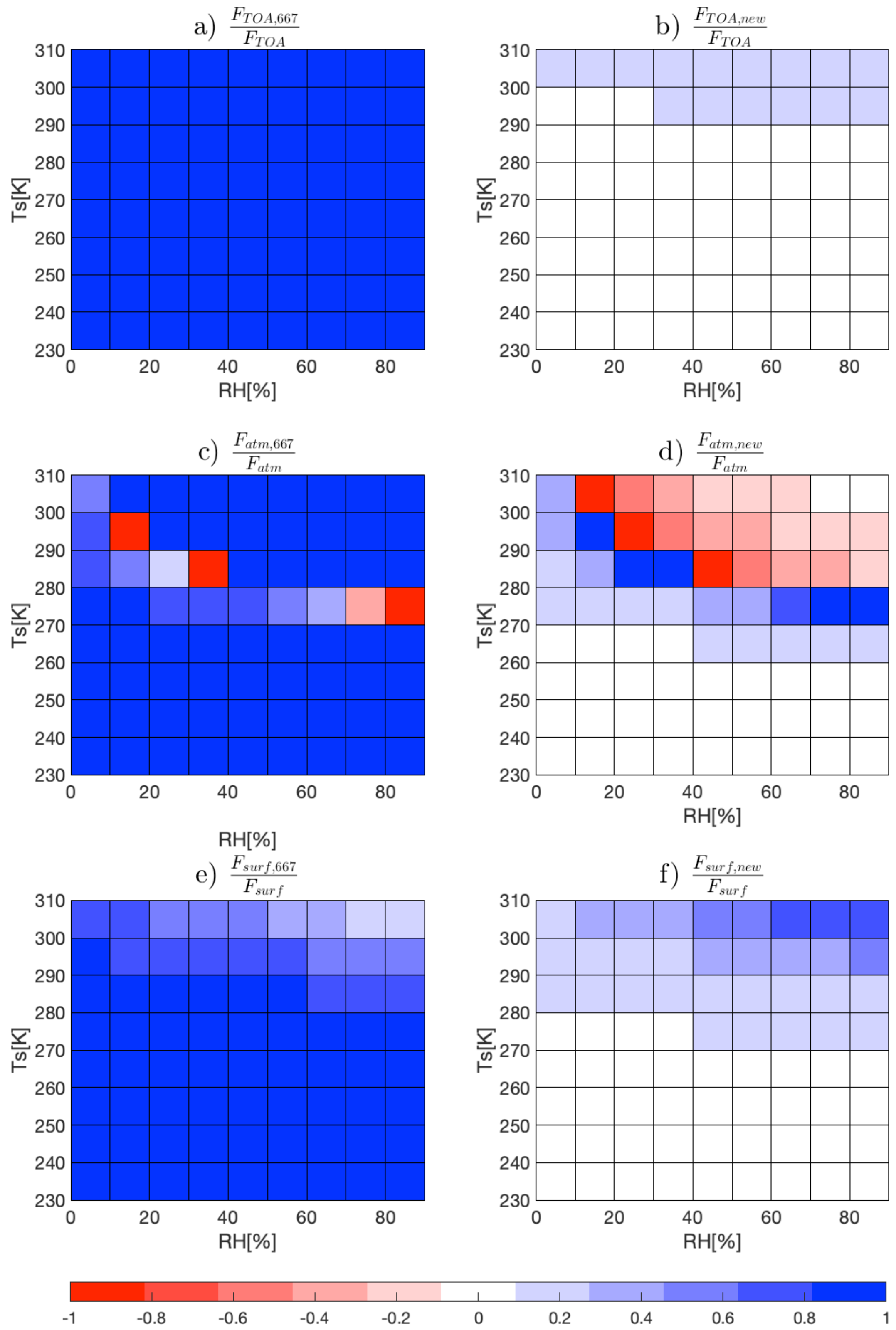

Figure S6. The proportion of each CO_2's two infrared bands (667 cm^{-1} band and the new band) contribution to F_{TOA} (a & b), F_{atm} (c & d), and F_{surf} (e & f) under climate state ranging

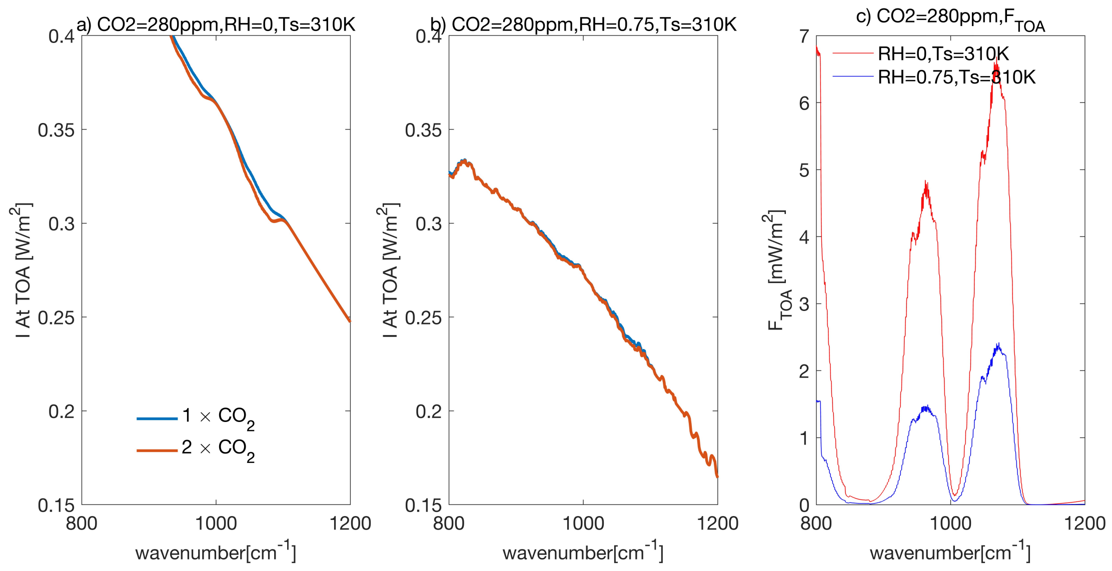

Figure S7. At TOA, the new CO_2 bands (a) Outgoing radiation for dry atmosphere with only CO_2 before and after CO_2 doubling. (b) Outgoing radiation for moist atmosphere with both CO_2 and H_2O before and after CO_2 doubling. (c) Comparison of TOA radiative forcing (FTOA) between the dry CO_2-only atmosphere and the combined CO_2+H_2O atmosphere.

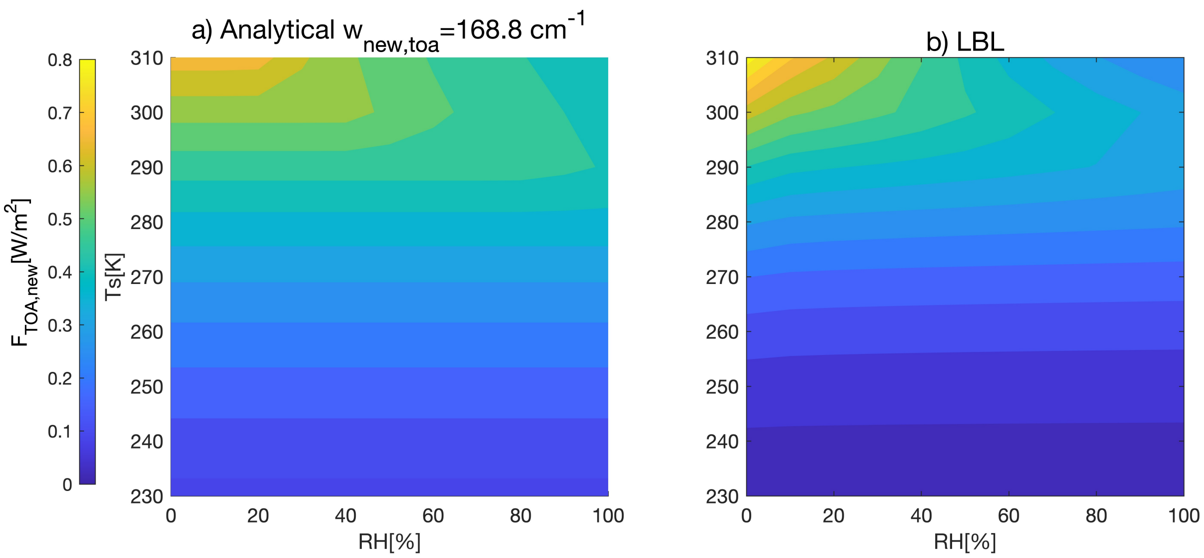

Figure S8. $F_{TOA,new}$ as a function of RH and T_s from a) the analytical model and b) the LBL simulation.

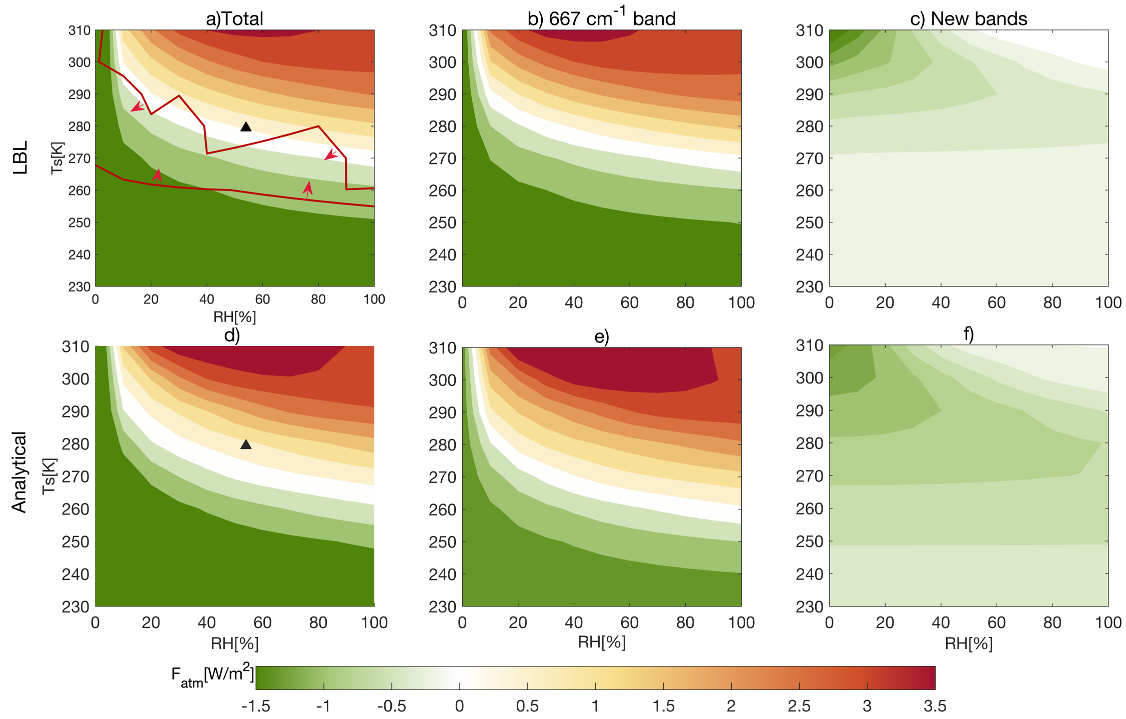

Figure S9. Same as Figure 3 but for F_{atm}. F_{atm} as a function of RH and T_s from LBL and our analytical model for F_{atm} considering the new bands (Equation 23&A.5). Black triangle: global-mean state. Red arrows: new bands accounting for more than 10% of the F_{atm}.

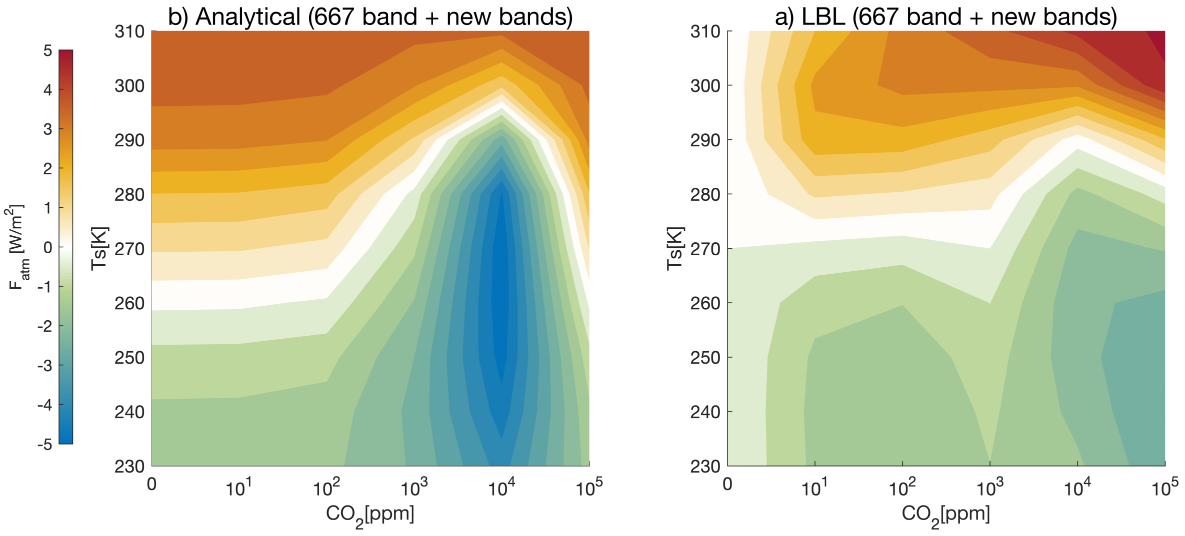

Figure S10. F_{atm} as a function of T_s and CO_2 at RH = 0.75 from a) the analytical model and b) the LBL simulation.

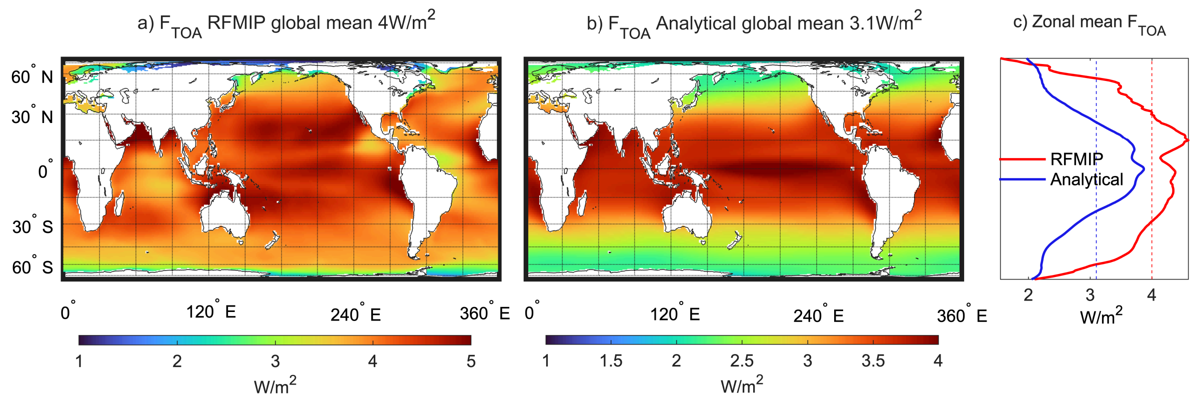

Figure S11. The distribution of F_{TOA} is presented for: a) the simulation results from RFMIP, b) the calculations using the Nadir analytical model, and c) the meridional average as a function of latitude. The initial conditions for all cases are based on the RFMIP pi-clim fields, consistent with the methodology described in Section 4.1.

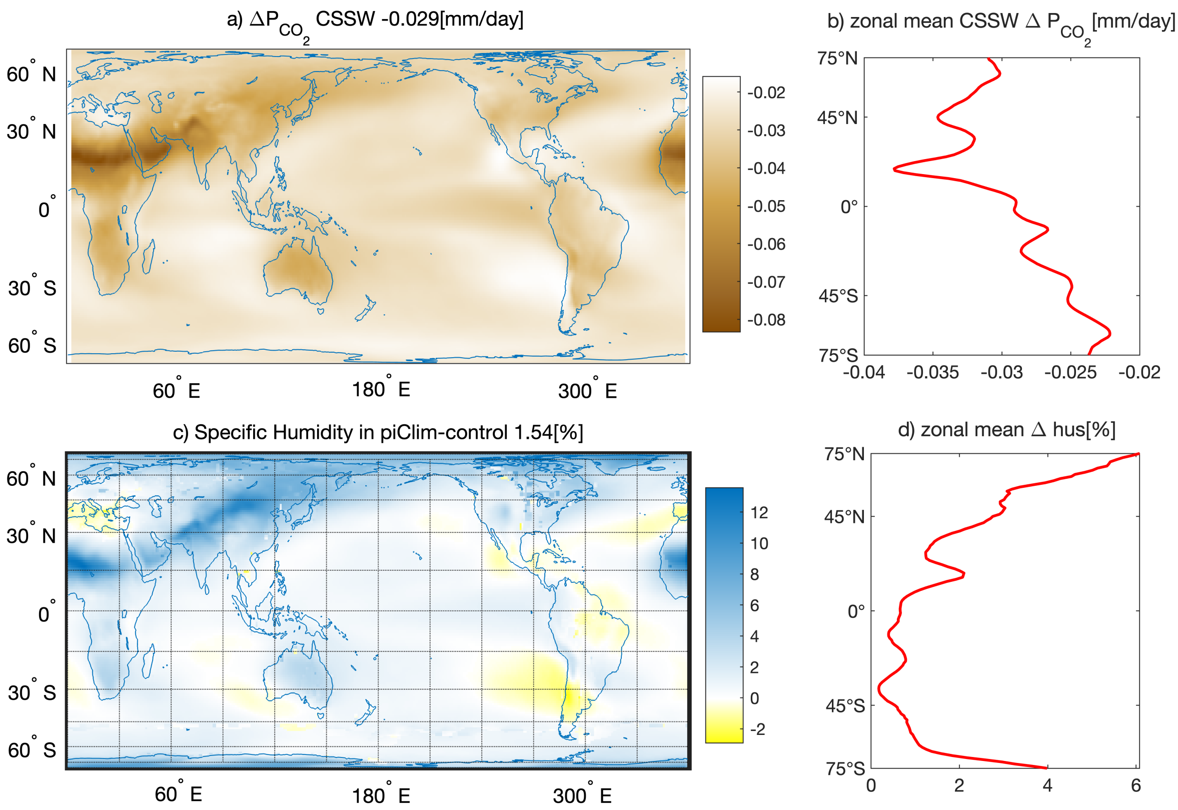

Figure S12. Spatial patterns of precipitation change caused by clear-sky shortwave(a) and percentage change in atmospheric column specific humidity (c), averaged over 15 RFMIP models. (b) and (d) are their zonal mean.

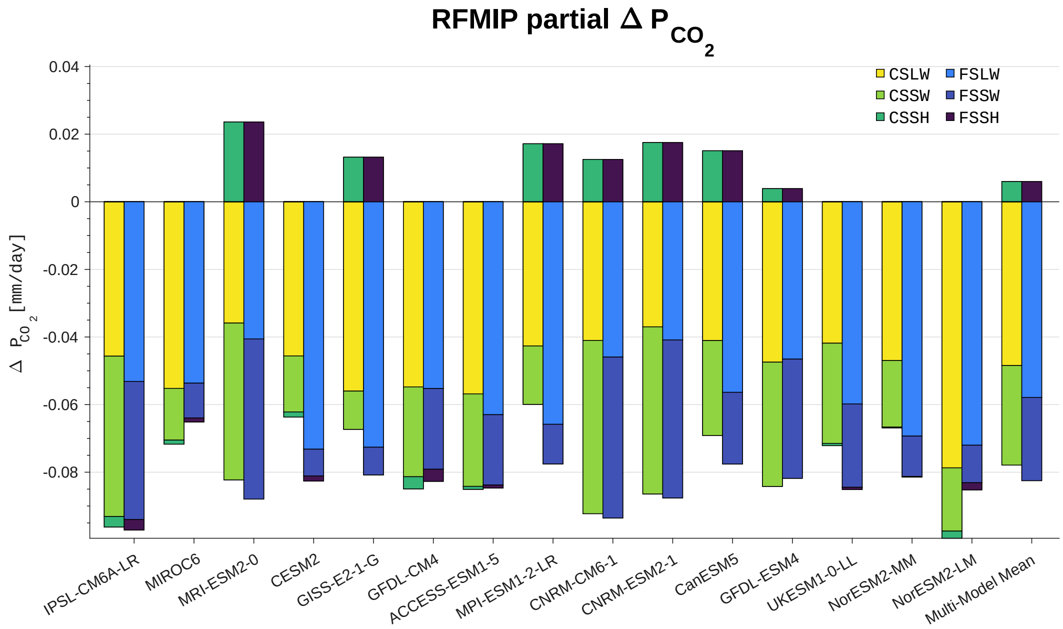

Figure S13. ΔP_{CO_2} resulting from longwave (LW), shortwave (SW), and sensible heat (SH) fluxes, as estimated under clear-sky(CS) and full-sky(FS) based on the energy balance from each CMIP model and their multi-model mean.

Table S2. The rate of precipitation change from CO_2 doubling contributed by clear-sky longwave forcing ($\frac{\Delta P_{CO_2} CSLW}{P}$) in 15 RFMIP models and their multi-model mean. Note: Since the T_s over land in RFMIP is not fixed, we only used ocean grids when calculating ΔP_{CO_2} CSLW. However, considering the global energy transport, we used all grids when calculating the original precipitation P.

Model \ Factor	ΔP_{CO_2} CSLW (mm/day)	P (mm/day)	$\frac{\Delta P_{CO_2} CSLW}{P}$ (%)
IPSL-CM6A-LR	-0.050	3.0	-1.7
MIROC6	-0.062	3.2	-2.0
MRI-ESM2-0	-0.046	3.0	-1.5
CESM2	-0.055	2.9	-1.9
GISS-E2-1-G	-0.070	3.0	-2.4
GFDL-CM4	-0.066	2.9	-2.3
ACCESS-ESM1-5	-0.065	3.2	-2.0
MPI-ESM1-2-LR	-0.052	2.8	-1.8
CNRM-CM6-1	-0.045	2.9	-1.6
CNRM-ESM2-1	-0.045	2.9	-1.5
CanESM5	-0.051	2.9	-1.8
GFDL-ESM4	-0.058	3.0	-2.0
UKESM1-0-LL	-0.045	3.1	-1.5
NorESM2-MM	-0.056	2.9	-2.0
NorESM2-LM	-0.087	2.9	-3.0
Multi-Model Mean	-0.057	3.0	-1.9

Table S3. Estimated Proportion of Decomposed ΔP_{CO_2} in 15 RFMIP Models under Clear-Sky and Cloudy-Sky Conditions

Factor / Model	CSLW	CSSW	CSSH	CS	FSLW	FSSW	FSSH	FS
IPSL-CM6A-LR	48%	50%	3%	100%	55%	43%	3%	101%
MIROC6	85%	24%	2%	111%	83%	16%	2%	100%
MRI-ESM2-0	51%	73%	-37%	92%	64%	74%	-37%	101%
CESM2	54%	20%	2%	76%	87%	9%	2%	98%
GISS-E2-1-G	65%	13%	-15%	63%	84%	9%	-15%	78%
GFDL-CM4	67%	32%	4%	103%	67%	30%	4%	101%
ACCESS-ESM1-5	68%	33%	1%	101%	75%	25%	1%	101%
MPI-ESM1-2-LR	71%	28%	-28%	71%	109%	19%	-28%	100%
CNRM-CM6-1	49%	62%	-15%	96%	55%	57%	-15%	98%
CNRM-ESM2-1	51%	68%	-24%	95%	56%	65%	-24%	97%
CanESM5	66%	45%	-24%	87%	91%	34%	-24%	100%
GFDL-ESM4	61%	48%	-5%	104%	60%	46%	-5%	101%
UKESM1-0-LL	50%	35%	1%	86%	71%	29%	1%	101%
NorESM2-MM	58%	24%	0	83%	86%	15%	0	101%
NorESM2-LM	93%	22%	2%	117%	85%	13%	2%	100%
Multi-Model Mean	62%	38%	-8%	92%	74%	32%	-8%	98%